INTERNATIONAL JOURNAL FOR NUMERICAL METHODS IN ENGINEERING
Int. J. Numer. Meth. Engng 2017; **00**:1–34
Published online in Wiley Online Library (www.onlinelibrary.wiley.com). DOI: 10.1002/nme.5571

Micro-macro concurrent topology optimization for nonlinear solids with a decoupling multi-scale analysis

Junji Kato[1]*, Daishun Yachi[1], Takashi Kyoya[1], Kenjiro Terada[2]

[1] *Department of Civil and Environmental Engineering, Tohoku University, 6-6-06, Aramaki, Aoba-ku, Sendai 980-8579, Japan*
[2] *International Research Institute of Disaster Science, Tohoku University, 468-1, Aramaki, Aoba-ku, Sendai 980-0845, Japan*

SUMMARY

The present study proposes a method of micro-macro concurrent topology optimization for a two-phase nonlinear solid to minimize the end compliance of its macrostructure undergoing large deformation. In order to reduce the computational costs to solve a two-scale boundary value problem (BVP) under geometrically nonlinear setting, we employ the so-called method of *decoupling multi-scale structural analysis*, in which the micro- and macroscopic BVPs are decoupled in terms of the homogenization process. An isotropic hyperelasticity model is employed for the constitutive model for microstructures, while an orthotropic one is assumed to represent the macroscopic material behavior. Owing to this decoupling framework, the micro-macro concurrent optimization problem can be split into two individual problems at the micro- and macro-scales for the sake of algorithmic simplicity. Also, a two-scale adjoint sensitivity analysis can be performed within the framework of computational homogenization. It is verified from a series numerical examples that the proposed method is capable of computing the optimal structures at both micro- and macro-scales, according to the level of applied load.

Received . . .

KEY WORDS: Multi-scale topology optimization, Decoupling multi-scale analysis, Nonlinear mechanics, Homogenization, Large deformation

*Correspondence to: J. Kato, Department of Civil and Environmental Engineering, Tohoku University, 6-6-06, Aramaki, Aoba-ku, Sendai 980-8579, Japan E-mail: junji.kato.a5@tohoku.ac.jp

Contract/grant sponsor: Publishing Arts Research Council; contract/grant number: 98–1846389

1. INTRODUCTION

Most structural materials can be regarded as composites from a micro-level perspective, and thereby their mechanical behavior is known to strongly depend on the micro-level geometric characteristics of constituent materials, such as layout, shape and dimensions. It is thus the common knowledge that the macroscopic material properties can be controlled to some degree by effectively arranging different types of constituents at the micro-scale. In the field of material development, in particular, much time and energy have been devoted to finding an optimal microstructure that can maximize the macroscopic mechanical performance or control its response as intended. To reduce such a uphill task, a numerical strategy, so-called topology optimization, has been drawing intense research interest because of its overwhelming flexibility in design in the past decades. Topology optimization already plays a significant role in design divisions of many industries, and nowadays is applied even for the design/development for advanced materials as reported in [1, 2, 3].

Directing our attention to manufacturing aspects, we notice that use of 3D printers in production and engineering, often called *additive manufacturing*, has recently become an increasingly realistic proposition. Discussions have been taking place on the possibility and potential of a new manufacturing framework that combines topology optimization-based design tools with additive manufacturing [4, 5, 6, 7]. Combining their advantages will enable manufacturing that focuses more on structural performance than on aspects of production. It should not be forgotten, however, that 3D printed products are still relatively unreliable in terms of strength of material, and thus further research and development is required. Nonetheless, reports have recently been released of free additive manufacture of metal macrostructures by controlling crystal orientation or crystal grain size in the micro-scale domain [8, 9, 10, 11]. If such technologies become established, material reliability will increase, enabling full-scale production with 3D printers. These trends indicate that the development of optimization methods for not only a macrostructure but also at the same time its microstructures will enable us to create a totally new product.

In this context, we focus on optimizing the topologies of both the micro- and macrostructures simultaneously, in order to maximize the mechanical performance of a macrostructure. In fact, recent years have seen a renewal of interest in the so-called concurrent multi-scale topology optimization. Rodrigues et al. [12] reported such an achievement in their research on maximization of stiffness of a linear elastic body. Yan et al. [13] introduced concurrent multi-scale topology optimization of a single microstructure, the so-called *uniformly-structured material*, for thermo-elastic structure. Niu et al. [14] proposed a method for simultaneous optimization of the topologies of both micro- and macrostructures for maximizing the lowest natural frequencies. Sivapuram et al. [15] also introduced concurrent multi-scale topology optimization based on a level set method considering the non-uniform structured material for a two-dimensional linearly elastic body. Some research groups make use of the Bi-directional Evolutionary Structural Optimization (BESO) method for the micro-macro concurrent topology optimization, e.g. Xia and Breitkopf [16], [17], Yan et al. [18].

To realize the above-mentioned multi-scale concurrent topology optimization, we need to solve a micro-macro coupled boundary value problem (BVP), known as *two-scale BVP*, which is composed of micro- and macroscopic BVPs within the framework of mathematical homogenization theory. The so-called multi-scale analysis to solve the two-scale BVP is often referred to as

the computational homogenization, and has provoked a great deal of controversy. Particularly for nonlinear problems, since the macroscopic constitutive equations cannot be provided in the macroscopic BVP, many studies have been reported so far for nonlinear computational homogenization, and various numerical techniques have been proposed, taking into account the material/geometrical nonlinear characteristics [19, 20, 21, 22]. These techniques, known as micro-macro coupled multi-scale analysis, or simply FE^2 methods, commonly require us to solve a microscopic BVP at each integration point in a finite element of a macrostructure in order to solve the macroscopic BVP and by necessity demand huge amount of computing time (and hence costs). Although we would enjoy a certain level of versatility and reliability of the coupled-type multi-scale analysis, being well supported by theory, the coupled-type multi-scale analysis methods can rarely be applied to practical designs, when nonlinear structural problems are considered. Inevitably, therefore, much more unrealistic computational effort is needed for topology optimization with the micro-macro coupled multi-scale analysis for nonlinear solids.

To the best of the present authors' knowledge, only few attempts have so far been made at the studies on the micro-macro concurrent multi-scale topology optimization involving nonlinearities. Nakshatrala et al. [23] proposed a method of multi-scale topology optimization based on micro-macro coupled multi-scale analysis for 2D problems using a Neo-Hookean model [24, 25], where the total material volume is constrained (net mass) without distinguishing between micro- and macro- material volume. In their study, the multilevel nested Newton method is employed to reduce the amount of calculation to some extent – which would otherwise be considerably costly and require further parallel computation with a certain number of processors to make the calculation time reasonable. Nonetheless, when considering 3D problems and/or problems with path-dependent constituents at the micro-scale, such as elastic-plastic materials, the multi-scale topology optimization with the use of the coupled-type multi-scale analysis is of almost no use especially from the viewpoint of practical design processes. Thus, more effective approaches to reduce the computational costs are needed for further developments of multi-scale topology optimization.

In these circumstances, Kato et al. [26] employed the so-called "decoupling multi-scale analysis" method [27, 28], which substantially reduces calculation costs, to obtain optimized topologies of microstructures subjected to macroscopic excitations. The method of decoupled-type multi-scale analysis is an approximate scheme to solve nonlinear two-scale BVP by making the micro- and macroscopic BVPs decoupled in terms of the homogenization process in analogy with linear computational homogenization. More specifically, in the decoupling method, the macroscopic constitutive equation, whose function form is generally not provided in the original two-scale BVP, is assumed with reference to the constitutive equations employed at the micro-scale. Then, its material parameters are determined by means of a certain appropriate optimization scheme, so that the paths of the constitutive equation would fit the results of a series of prescribed microscopic analyses, called *numerical material tests* (NMTs). This process to find values of the material parameters is called *parameter identification* in this study.

Accordingly, the decoupling method is not only superlatively practical over the afore-mentioned coupled-type methods, but also highly versatile, once we can ensure the conformity between the assumed macroscopic constitutive equation and the actual macroscopic material behavior realized by NMTs. Of course, the reliability also hinges on the accuracy of parameter identification, the

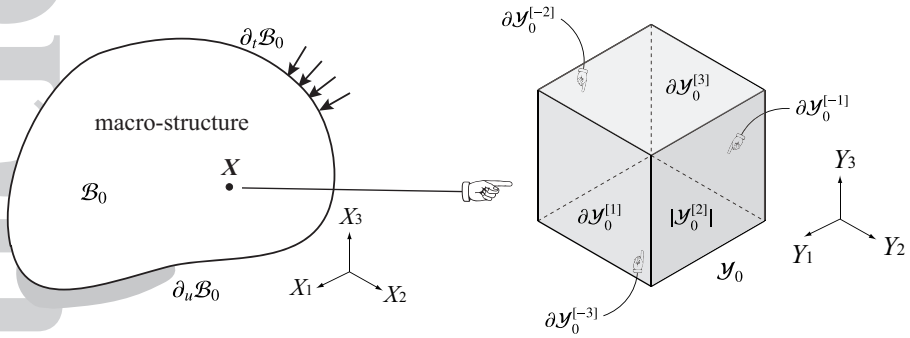

Figure 1. Micro- and macroscopic domains with their own coordinate systems.

decoupling method is amenable to various nonlinear material models and geometrical nonlinear problems; see Terada et al. [29] for application to inelastic materials.

In this study, by exploiting the capability of the decoupling multi-scale analysis, we develop a method of concurrent multi-scale topology optimization for 3D nonlinear solids undergoing large deformation. The macroscopic end compliance is taken as an objective function to be minimized in the present optimization problem under the equality constraint condition that both values of micro- and macroscopic material volume are fixed. For algorithmic simplicity, the micro-macro concurrent optimization problem is split into two individual problems at the micro- and macro-scales. Also, an adjoint sensitivity analysis is carried out within the framework of a computational homogenization so that the present optimization problem can be solved with reasonable computational efforts. It is, however, noted that we sometimes suffer from the drawback in ensuring the stability of convergence to an optimum solution, which is caused by the failure of parameter identification for the assumed macroscopic constitutive equation and/or by the inconsistency of the actual macroscopic material behavior with the assumed macroscopic constitutive equation. The countermeasure against this drawback will also be described for gaining numerical robustness.

The so-called density-based topology optimization is utilized in this study, where the microstructure is assumed to be *uniformly-structured composite material* consisting of two different solids: the one is soft and the other stiff hyperelastic materials, and where the macrostructure is assumed to be a *porous material* represented by the continuous "0-1" ("void–mixture") interpolation scheme. It should be noted, however, that the proposed method does not limit the number of microstructures, that is, it can be extended to cases allowing a distribution of different optimized microstructures throughout the optimized macroscopic domain without any special operation. The performance of the proposed method is verified with some numerical examples. In each of them, two cases with different levels of applied loading are tested to observe the difference between the two sets of optimized topologies of micro- and macrostructures; one is small enough to assume infinitesimally small deformation and the other large enough to induce severely large deformation. In these numerical examples, the Mooney-Rivlin model is employed as the micro-scale constitutive equation for an isotropic hyperelastic body, and its orthotropic version proposed by Kaliske [30] and Kaliske and Schmidt [31] is assumed for the macroscopic constitutive equation.

2. DECOUPLING MULTI-SCALE ANALYSIS

In this section, we summarize the method of decoupling multi-scale analysis as an approximation scheme to effectively solve a two-scale BVP. After the two-scale BVP is described within the framework of finite strain theory, the outline and the step-by-step procedure of the decoupling analysis are briefly explained.

2.1. Two-scale boundary value problem

The two-scale BVP for a heterogeneous medium or composite material is formally derived through the formulation in homogenization theory, and is commonly composed of micro- and macroscopic BVPs, which have their own analysis domains endowed with separate spatial coordinate systems at micro- and macro-scales; see Figure 1. The micro- and macroscopic domains are respectively denoted by $\mathcal{Y}_0$ and $\mathcal{B}_0$ in the initial configurations, and their coordinate systems by $\boldsymbol{Y}$ and $\boldsymbol{X}$. A microscopic analysis domain of a periodic representative volume element is often referred to as a unit cell in computational homogenization and so is hereafter.

The unit cell is assumed to be a rectangular parallelepiped and its boundary surface $\partial\mathcal{Y}_0{}^{[k]}$ is placed parallel to the microscopic coordinate axis Y_k having orthonormal basis vector $\boldsymbol{e}^{[k]}$ as its normal vector. Then, the position vector $\boldsymbol{Y}$ in the initial configuration $\mathcal{Y}_0$ of the unit cell is identified with that in the current configuration $\mathcal{Y}$ with the microscopic motion $\boldsymbol{y} = \varphi(\boldsymbol{Y}) = \boldsymbol{Y} + \boldsymbol{w}(\boldsymbol{X}, \boldsymbol{Y})$. Here, $\boldsymbol{w}(\boldsymbol{X}, \boldsymbol{Y})$ is the microscopic displacement field, which depends on both the micro- and macro-scales. The detailed explanation for $\boldsymbol{w}(\boldsymbol{X}, \boldsymbol{Y})$ is referred to [28], which the present study follows.

With the macro-scale $\boldsymbol{X}$ being a parameter, the microscopic deformation gradient is defined as

$$\boldsymbol{F}_{\mathrm{m}}(\boldsymbol{X}, \boldsymbol{Y}) = \nabla_Y \varphi((\boldsymbol{X}, \boldsymbol{Y})) = \nabla_Y \boldsymbol{w}(\boldsymbol{X}, \boldsymbol{Y}) + \boldsymbol{1}. \tag{1}$$

The microscopic equilibrium equation is

$$\nabla_Y \cdot \boldsymbol{P}_{\mathrm{m}} = \boldsymbol{0}, \tag{2}$$

where $\boldsymbol{P}_{\mathrm{m}}$ is the microscopic 1st Piola-Kirchhoff (PK1) stress and is determined by appropriate constitutive equations for the constituent materials. Note that although hyperelastic materials are assumed in this study, any type of material models can be employed. Then, the microscopic BVP for the unit cell consists of Equations (1), (2) and selected constitutive equations along with the boundary conditions on external surfaces $\partial\mathcal{Y}_0^{[\pm k]}$ $(k = 1, 2, 3)$ on the unit cell as

$$\boldsymbol{w}^{[k]} - \boldsymbol{w}^{[-k]} = \tilde{\boldsymbol{H}}(\boldsymbol{X}) \cdot (\boldsymbol{Y}^{[k]} - \boldsymbol{Y}^{[-k]}) = \tilde{\boldsymbol{H}}(\boldsymbol{X}) \cdot \boldsymbol{L}^{[k]}. \tag{3}$$

Here, we have defined $(\bullet)^{[\pm k]} := (\bullet)|_{\partial\mathcal{Y}_0^{[\pm k]}}$, and $\boldsymbol{L}^{[k]}$ is a vector connecting the corresponding pairs of nodes, whose position vectors are denoted by $\boldsymbol{Y}^{[\pm k]}$, in parallel to the Y_k-direction, and is referred to as the *side vector*. Also, $\tilde{\boldsymbol{H}}(\boldsymbol{X})$ is the macroscopic displacement gradient, which is independent of $\boldsymbol{Y}$, and will be described below. The treatment of Equation (3) in the actual computation is explained in Appendix A.

Meanwhile, denoting the initial and current configurations of the macroscopic analysis domain by $\mathcal{B}_0$ and $\mathcal{B}$, respectively, we define the motion from $\mathcal{B}_0$ to $\mathcal{B}$ such that $\boldsymbol{x} = \tilde{\varphi}(\boldsymbol{X}) \in \mathcal{B}$. Then, the

macroscopic deformation gradient is defined as $\boldsymbol{F}_{\mathrm{M}}(\boldsymbol{X}) = \tilde{\boldsymbol{H}}(\boldsymbol{X}) + \mathbf{1}$, and is known to be equal to the volume-averaged microscopic deformation gradient as

$$\boldsymbol{F}_{\mathrm{M}}(\boldsymbol{X}) = \frac{1}{|Y|}\int_{\mathcal{Y}_0} \boldsymbol{F}_{\mathrm{m}}(\boldsymbol{X},\boldsymbol{Y})\mathrm{d}Y = \tilde{\boldsymbol{H}}(\boldsymbol{X}) + \mathbf{1}, \tag{4}$$

where $|Y|$ represents the volume of the unit cell in the initial configuration $\mathcal{Y}_0$. Similarly, the macroscopic PK1 stress $\boldsymbol{P}_{\mathrm{M}}$ is the volume-averaged microscopic stress as

$$\boldsymbol{P}_{\mathrm{M}}(\boldsymbol{X}) = \frac{1}{|Y|}\int_{\mathcal{Y}_0} \boldsymbol{P}_{\mathrm{m}}(\boldsymbol{X},\boldsymbol{Y})\mathrm{d}Y, \tag{5}$$

and is supposed to satisfy the following equilibrium equation for the macrostructure:

$$\nabla_X \cdot \boldsymbol{P}_{\mathrm{M}} = \mathbf{0}. \tag{6}$$

Here, the body force is neglected for simplicity. Thus, the macroscopic BVP consists of Equations (4), (5) and (6) along with appropriate essential and natural boundary conditions on $\partial_u\mathcal{B}_0$ and $\partial_t\mathcal{B}_0$, respectively.

It should be noted that the macroscopic BVP is coupled with the solution of the microscopic BVP associated with $\boldsymbol{X}$. This implies that the macroscopic stress can be determined without any specific macroscopic constitutive equation. In other words, homogenization theory generally does not provide any function form to evaluate the macroscopic stress in nonlinear problems. The solution method to solve the two-scale BVP directly is called the micro-macro coupled multi-scale analysis, or simply FE^2 method, which commonly requires us to solve a microscopic BVP at each integration point in a macroscopic finite element model to evaluate the macroscopic stress, and by necessity demands huge amount of computing costs. However, when the macroscopic constitutive equation is analogized with the ones employed at the micro-scale, the micro- and macroscopic BVPs can be decoupled. The next subsection summarizes the decoupling scheme in this direction.

2.2. Outline of decoupling multi-scale analysis

We outline the method of decoupling multi-scale analysis as an approximation scheme to effectively solve a two-scale BVP defined above. The procedure is presented below in order.

(i) With reference to the constitutive equations employed for the unit cell's constituents, we select the macroscopic constitutive equation that properly represents the macroscopic material behavior of the composite material under consideration. As a matter of policy, the macroscopic material response is expected to partially inherit the microscopic ones. That is, if neo-Hookean-type isotropic hyperelastic materials are employed at the micro-scale, the function form of the macroscopic constitutive equation is supposed to be the same type except that it may reveal anisotropy. Since this is indeed the case in this study, we select the anisotropic version of the neo-Hookean model as the macroscopic constitutive equation. The concrete function forms of the micro- and macroscopic constitutive equations are detailed in Appendix B.

(ii) Preparing several patterns of typical macroscopic deformation modes represented by $\tilde{\boldsymbol{H}}$ in Equation (3), we carry out a series of numerical analyses to solve the microscopic BVP. Then, the evaluated microscopic stresses are converted to the macroscopic ones with the averaging relation (5) to obtain the macroscopic stress-strain curves, which can be virtually regarded as 'empirical' data. This set of processes, which is nothing but computational homogenization, is called the *numerical material testing* (NMT) in this study as mentioned before, and sometimes virtual testing elsewhere. Some technical issues for NMTs are presented in Appendix A.

(iii) Using the relationships between the macroscopic stresses and strains obtained by NMTs as measured data, we try to determine the material parameters of the assumed macroscopic constitutive equation with the help of a certain optimization scheme. It should be noted that the optimization scheme to be employed here is different from the optimization algorithm used to update design variables in topology optimization. In this study, the differential evolution (DE) method [32], known to be a particularly high performing optimization algorithm in terms of calculation speed and accuracy, is employed. The specific identification methodology with DE is outlined in Appendix A and more details of DE are found in the reference [32].

(iv) Using the identified macroscopic material parameters, we solve the macroscopic BVP with appropriate boundary conditions. After the analysis, macroscopic deformation histories at given material points in the macrostructure are extracted as necessary, and then provided as data to the microscopic BVPs to evaluate the microscopic responses corresponding to the macroscopic material responses at the selected points. This process is sometimes referred to as the *localization* after the fashion of mathematical homogenization and is effectively utilized in the micro-macro concurrent topology optimization proposed in this study.

More detailed explanation of the analysis procedure and the concrete process of NMT is referred to Reference [28].

3. MICRO-MACRO CONCURRENT TOPOLOGY OPTIMIZATION

This section presents the formulation of micro-macro concurrent topology optimization that enjoys the efficiency of the decoupling multi-scale analysis. After defining the micro- and macroscopic design variables and introducing the relaxed variations of the respective associated elastic potentials (or stored strain energy functions), we formulate the multi-scale concurrent optimization problem and then propose a two-scale adjoint sensitivity analysis.

3.1. Microscopic design variables and relaxation of effective elastic potential

The present study employs the concept of the SIMP method [33] to define the design variables in microstructure and relaxes the elastic potentials that carry material responses as in the study by [23]. Since the SIMP method was originally devised to deal with a single, porous material, it cannot be directly applied to our present optimization policy, in which a unit cell is supposed to be composed of two different materials. Therefore, the two-phase-material optimization method [34], which was developed along the lines of the SIMP method, is employed so as to be applicable to composites in this study. This SIMP-like method replaces the set of "void" and "solid" in the original SIMP

method by two separate solid materials, phase-1 and phase-2, respectively. Thus, when a unit cell is composed of phases-1 and 2, the microscopic design variable s_i is defined as the volume fraction of phase-2 in element i of the unit cell's finite element (FE) model, which takes values between 0 and 1. In other words, the i-th element is occupied by phase-1 when $s_i = 0$, while occupied by phase-2 when $s_i = 1$. When $0 < s_i < 1$, the material is regarded as a mixture of the two phases.

Using the design variables defined above, we approximate the "effective" *microscopic* elastic potential for element i by the following interpolation on the basis of the rule of mixture:

$$\Psi_{\mathrm{m}} = (1 - s_i^{\eta})\Psi_1 + s_i^{\eta}\Psi_2. \tag{7}$$

Here, Ψ_1 and Ψ_2 represent the elastic potentials of isotropic hyperelastic materials, phase-1 and phase-2, respectively, and η is the power to control the interpolation. In this formulation, phase-2 is assumed to be stiffer than phase-1. Then, the partial differentiation of Ψ_{m} with respect to the microscopic deformation gradient $\boldsymbol{F}_{\mathrm{m}}$ yields the microscopic PK1 stress $\boldsymbol{P}_{\mathrm{m}}$ as

$$\boldsymbol{P}_{\mathrm{m}} = \frac{\partial \Psi_{\mathrm{m}}}{\partial \boldsymbol{F}_{\mathrm{m}}} = (1 - s_i^{\eta})\frac{\partial \Psi_1}{\partial \boldsymbol{F}_{\mathrm{m}}} + s_i^{\eta}\frac{\partial \Psi_2}{\partial \boldsymbol{F}_{\mathrm{m}}} = (1 - s_i^{\eta})\boldsymbol{P}_1 + s_i^{\eta}\boldsymbol{P}_2. \tag{8}$$

Here, $\boldsymbol{P}_1$ and $\boldsymbol{P}_2$ indicate the microscopic PK1 stress of phase-1 and phase-2, respectively, which can be uniquely determined once $\boldsymbol{F}_{\mathrm{m}}$ is given.

3.2. Macroscopic design variables and relaxation of effective elastic potential

In contrast to the unit cell, the macrostructure considered in this study is made from a single homogenous material so that the SIMP method can be applied. When material density ρ_I ($0 < \rho_I \leq 1$), which is equivalent to the material's volume fraction of each finite element I, is taken as the macroscopic design variable, the "effective" *maroscopic* elastic potential can be of the following form:

$$\bar{\Psi}_{\mathrm{M}} = \rho_I^{\eta}\Psi_{\mathrm{M}}, \tag{9}$$

where Ψ_{M} is the macroscopic elastic potential, which is expected to represent anisotropic hyperelastic material behavior. By partially differentiating this potential with respect to the macroscopic deformation gradient $\boldsymbol{F}_{\mathrm{M}}$, we obtain the effective macroscopic PK1 stress as

$$\bar{\boldsymbol{P}}_{\mathrm{M}} = \frac{\partial \bar{\Psi}_{\mathrm{M}}}{\partial \boldsymbol{F}_{\mathrm{M}}} = \rho_I^{\eta}\frac{\partial \Psi_{\mathrm{M}}}{\partial \boldsymbol{F}_{\mathrm{M}}} = \rho_I^{\eta}\boldsymbol{P}_{\mathrm{M}}, \tag{10}$$

which is also identified with

$$\bar{\boldsymbol{P}}_{\mathrm{M}} = \frac{\rho_I^{\eta}}{|Y|}\int_{\mathcal{Y}_0}\left\{(1 - s_i^{\eta})\boldsymbol{P}_1 + s_i^{\eta}\boldsymbol{P}_2\right\}\mathrm{d}Y, \tag{11}$$

reflecting the relationships (5) and (8). In analogy with this, Equation (9) can also be rewritten as

$$\begin{aligned}\bar{\Psi}_{\mathrm{M}} &= \frac{\rho_I^\eta}{|Y|}\int_{\mathcal{Y}_0}\Psi_{\mathrm{m}}\mathrm{d}Y \\ &= \frac{\rho_I^\eta}{|Y|}\int_{\mathcal{Y}_0}\left\{(1-s_i^\eta)\Psi_1 + s_i^\eta\Psi_2\right\}\mathrm{d}Y.\end{aligned} \tag{12}$$

As can be seen in these equations, the effective macroscopic PK1 stress $\bar{\boldsymbol{P}}_{\mathrm{M}}$ and the effective macroscopic potential $\bar{\Psi}_{\mathrm{M}}$ can be expressed so as to depend on both the micro and macro design variables.

3.3. Two-scale optimization problem

Using the sets of micro- and macroscopic design variables, $\boldsymbol{\rho}$ and $\boldsymbol{s}$, defined above, we pose a two-scale optimization problem to minimize the end compliance of a macrostructure (i.e., maximization of stiffness in the final loading step). Within the present two-scale framework, the two-scale objective function can be expressed as $f(\boldsymbol{U},\boldsymbol{s},\boldsymbol{\rho})$, in which $\boldsymbol{U} := \boldsymbol{x} - \boldsymbol{X}$ is the macroscopic displacement field associated with the motion $\tilde{\varphi}(\boldsymbol{X}) \in \mathcal{B}$, and at the same time the equality constraints are imposed on both the micro- and macroscopic design variables under the constraint of fixed material volume. In this study, macroscopic constraint $h_{\mathrm{M}}(\boldsymbol{\rho}) = 0$ requires that the material volume in the macrostructure be fixed at a prescribed value $\hat{V}_{\mathrm{M}}$, whereas microscopic constraint $h_{\mathrm{m}}(\boldsymbol{s}) = 0$ indicates that the original volume $\hat{V}_{\mathrm{m}}$ of phase-2 in a unit cell does not change for the entire unit cell during optimization. Under these conditions, the following optimization problem can be posed:

$$\min\ f(\boldsymbol{U},\boldsymbol{s},\boldsymbol{\rho}) = \int_{\partial\mathcal{B}_0}\hat{\boldsymbol{T}}_{\mathrm{M}}\cdot\boldsymbol{U}\mathrm{d}\Gamma, \tag{13}$$

subject to:

$$\boldsymbol{R}_{\mathrm{M}}(\boldsymbol{U},\boldsymbol{s},\boldsymbol{\rho}) = \boldsymbol{F}_{\mathrm{int}}(\boldsymbol{U},\boldsymbol{s},\boldsymbol{\rho}) - \boldsymbol{F}_{\mathrm{ext}} = \boldsymbol{0}, \tag{14}$$

$$h_{\mathrm{M}}(\boldsymbol{\rho}) = \int_{\mathcal{B}_0}\rho_I\mathrm{d}\Omega - \hat{V}_{\mathrm{M}} = 0, \qquad 0 < \rho_I \le 1, \quad I = 1,\ldots,n_\rho, \tag{15}$$

$$h_{\mathrm{m}}(\boldsymbol{s}) = \int_{\mathcal{Y}_0}s_i\mathrm{d}Y - \hat{V}_{\mathrm{m}} = 0, \qquad 0 \le s_i \le 1, \quad i = 1,\ldots,n_{\mathrm{s}}, \tag{16}$$

where n_ρ and n_{s} respectively represent the numbers of elements in the FE models of the macrostructure and the unit cell. Here, $\boldsymbol{R}_{\mathrm{M}}$ is the residual force vector of the macroscopic FE equilibrium equation defined with the nodal internal and external force vectors that are respectively defined as

$$\boldsymbol{F}_{\mathrm{int}} = \int_{\mathcal{B}_0}\boldsymbol{B}_0^{\mathrm{T}}\bar{\boldsymbol{P}}_{\mathrm{M}}\mathrm{d}\Omega, \quad \boldsymbol{F}_{\mathrm{ext}} = \int_{\partial\mathcal{B}_0}\boldsymbol{N}^{\mathrm{T}}\hat{\boldsymbol{T}}_{\mathrm{M}}\mathrm{d}\Gamma, \tag{17}$$

in which $\hat{\boldsymbol{T}}_{\mathrm{M}}$ is the macroscopic traction force vector applied on the external boundary of the macrostructure. Also, $\boldsymbol{N}$ and $\boldsymbol{B}_0$ are the matrices containing standard shape functions and their derivatives with respect to the macroscopic material coordinate system $\boldsymbol{X}$ [35], respectively. For the sake of simplicity, it is assumed that the body force is negligible and that the external vector $\boldsymbol{F}_{\mathrm{ext}}$ is independent of the macroscopic deformation and of all the design variables s_i and ρ_I.

In this study, we separate the two-scale optimization problem described above into two, which are exclusively associated with macro- and microscopic design variables, as follows:

• Optimization problem 1 (for macrostructure)

$$\min \ f(\boldsymbol{U}, \boldsymbol{\rho}; \hat{\boldsymbol{s}}) = \int_{\partial \mathcal{B}_0} \hat{\boldsymbol{T}}_{\mathrm{M}} \cdot \boldsymbol{U} \mathrm{d}\Gamma, \tag{18}$$

subject to:

$$\boldsymbol{R}_{\mathrm{M}}(\boldsymbol{U}, \boldsymbol{\rho}; \hat{\boldsymbol{s}}) = \boldsymbol{0}, \tag{19}$$

$$h_{\mathrm{M}}(\boldsymbol{\rho}) = \int_{\mathcal{B}_0} \rho_I \mathrm{d}\Omega \ - \ \hat{V}_{\mathrm{M}} \ = \ 0, \quad 0 < \rho_I \leq 1, \quad I = 1, ..., n_\rho. \tag{20}$$

• Optimization problem 2 (for unit cell)

$$\min \ f(\boldsymbol{U}, \boldsymbol{s}; \hat{\boldsymbol{\rho}}) = \int_{\partial \mathcal{B}_0} \hat{\boldsymbol{T}}_{\mathrm{M}} \cdot \boldsymbol{U} \mathrm{d}\Gamma, \tag{21}$$

subject to:

$$\boldsymbol{R}_{\mathrm{M}}(\boldsymbol{U}, \boldsymbol{s}; \hat{\boldsymbol{\rho}}) = \boldsymbol{0}, \tag{22}$$

$$h_{\mathrm{m}}(\boldsymbol{s}) = \int_{\mathcal{Y}_0} s_i \mathrm{d}Y \ - \ \hat{V}_{\mathrm{m}} \ = \ 0, \quad 0 \leq s_i \leq 1, \quad I = 1, ..., n_{\mathrm{s}}. \tag{23}$$

With the fixed design variable $\hat{\bullet}$, each of these optimization problems is solved separately in the same optimization step and the both micro- and macroscopic design variables are updated.

At this point, the concern for readers may be whether the important hierarchical and mechanical relationships between the different scales could be maintained and also whether these relationships could be reflected to the optimization results by separating the original optimization problem. However, as can be seen in Equations (18) to (23), the objective function is unique (common for the two sub-problems and not separated) and only equality constraints are simply separated with respect to two kinds of design variables, s_i and ρ_I, which are independent of each other. With this problem setting, changes of the microstructure (change of design variable s_i) will result in changes in the NMT data, leading to changes in fitted macro-scale constitutive parameters and thus changes in macro-scale response and eventually changes the objective function values. This implies that the important hierarchical and mechanical relationships between the different scales can be maintained and also reflected to the optimization results. To the best of the authors' knowledge, this solution method may be somehow related to the so-called *dual angular structure* described in Lasdon [36], which is a classical scheme but still in use today as basis of multi-level optimization and multi-disciplinary optimization.

To solve the two-scale optimization problem posed above, the optimality criteria (OC) method [37], a gradient-based method, is utilized as an effective optimization algorithm. Since the problem is separated as explained above, the OC method also has to be applied alternatively to update the macro and microscopic design variables.

As a reference, Figure 2 presents the overall flow of the proposed concurrent multi-scale topology optimization. The sensitivity analysis shown in this figure will be described in detail in the next section.

4. TWO-SCALE SENSITIVITY ANALYSIS

On the basis of the above formulation of the two-scale optimization problem, the two-scale sensitivity analysis is presented in this subsection. To facilitate efficient derivation of the sensitivity of the objective function, we employ the discrete adjoint method, in which the macroscopic equilibrium equation (14) is utilized. Subject to the decoupling multi-scale analyses, some remarks on the accuracy are also addressed.

4.1. Adjoint sensitivity analysis

The new objective function for the adjoint method is defined as

$$f' = f - \boldsymbol{\lambda}^{\mathrm{T}} \boldsymbol{R}_{\mathrm{M}} \tag{24}$$

$$= \boldsymbol{F}_{\mathrm{ext}}^{\mathrm{T}} \boldsymbol{U} - \boldsymbol{\lambda}^{\mathrm{T}} \left(\underbrace{\boldsymbol{F}_{\mathrm{int}}(\boldsymbol{U}) - \boldsymbol{F}_{\mathrm{ext}}}_{\boldsymbol{R}_{\mathrm{M}}=\boldsymbol{0}} \right), \tag{25}$$

where $\boldsymbol{\lambda}$ is the adjoint vector. This definition does not cause any mathematical problem as the value in parentheses is identically zero. Then, the sensitivity of the objective function with respect to the design variables is readily derived below in view of its dependencies on the micro- and macroscopic design variables.

First, the differentiation of Equation (25) with the macroscopic design variable ρ_I yields

$$\begin{aligned} \frac{\partial f}{\partial \rho_I} = \frac{\partial f'}{\partial \rho_I} &= \boldsymbol{F}_{\mathrm{ext}}^{\mathrm{T}} \frac{\mathrm{d}\boldsymbol{U}}{\mathrm{d}\rho_I} - \boldsymbol{\lambda}^{\mathrm{T}} \left(\frac{\partial \boldsymbol{R}_{\mathrm{M}}}{\partial \boldsymbol{U}} \frac{\mathrm{d}\boldsymbol{U}}{\mathrm{d}\rho_I} + \frac{\partial \boldsymbol{R}_{\mathrm{M}}}{\partial \rho_I} \right) \\ &= \left(\boldsymbol{F}_{\mathrm{ext}}^{\mathrm{T}} - \boldsymbol{\lambda}^{\mathrm{T}} \frac{\partial \boldsymbol{R}_{\mathrm{M}}}{\partial \boldsymbol{U}} \right) \frac{\mathrm{d}\boldsymbol{U}}{\mathrm{d}\rho_I} - \boldsymbol{\lambda}^{\mathrm{T}} \frac{\partial \boldsymbol{R}_{\mathrm{M}}}{\partial \rho_I}. \end{aligned} \tag{26}$$

Since the adjoint vector $\boldsymbol{\lambda}$ can arbitrarily be chosen, let us set it at $\boldsymbol{\lambda}^*$ that satisfies

$$\boldsymbol{K}_{\mathrm{T}}^{\mathrm{T}} \boldsymbol{\lambda}^* = \boldsymbol{F}_{\mathrm{ext}}, \tag{27}$$

so that the implicit sensitivity term $\mathrm{d}\boldsymbol{U}/\mathrm{d}\rho_I$ can be eliminated. Here, $\boldsymbol{K}_{\mathrm{T}}$ represents the tangent stiffness matrix when the macroscopic equilibrium condition is satisfied at the final loading step. Then, in view of Equation (11), the sensitivity with respect to ρ_I becomes

$$\begin{aligned} \frac{\partial f}{\partial \rho_I} &= -\boldsymbol{\lambda}^{*\mathrm{T}} \frac{\partial \boldsymbol{R}_{\mathrm{M}}}{\partial \rho_I} = -\boldsymbol{\lambda}^{*\mathrm{T}} \int_{\mathcal{B}_0} \boldsymbol{B}_0^{\mathrm{T}} \frac{\partial \bar{\boldsymbol{P}}_{\mathrm{M}}}{\partial \rho_I} \mathrm{d}\Omega \\ &= -\boldsymbol{\lambda}^{*\mathrm{T}} \int_{\mathcal{B}_0} \boldsymbol{B}_0^{\mathrm{T}} \left(\eta \rho_I^{\eta-1} \boldsymbol{P}_{\mathrm{M}} \right) \mathrm{d}\Omega, \end{aligned} \tag{28}$$

which can be evaluated, once we obtain the adjoint vector $\boldsymbol{\lambda}^*$ that satisfies Equation (27) and the macroscopic PK1 stress $\boldsymbol{P}_{\mathrm{M}}$ that satisfies the macroscopic equilibrium condition at the final loading step.

In a similar fashion, the sensitivity of the objective function with respect to the microscopic design variable s_i can be derived as follows

$$\begin{aligned}\frac{\partial f}{\partial s_i} &= -\boldsymbol{\lambda}^{*\mathrm{T}}\frac{\partial \boldsymbol{R}_{\mathrm{M}}}{\partial s_i} = -\boldsymbol{\lambda}^{*\mathrm{T}}\int_{\mathcal{B}_0}\boldsymbol{B}_0^{\mathrm{T}}\frac{\partial \bar{\boldsymbol{P}}_{\mathrm{M}}}{\partial s_i}\mathrm{d}\Omega \\ &= -\boldsymbol{\lambda}^{*\mathrm{T}}\int_{\mathcal{B}_0}\boldsymbol{B}_0^{\mathrm{T}}\left(\rho_I^{\eta}\frac{\partial \boldsymbol{P}_{\mathrm{M}}}{\partial s_i}\right)\mathrm{d}\Omega. \end{aligned} \tag{29}$$

Furthermore, in view of the homogenization formula (5) and the interpolated elastic potential (8), the sensitivity of the mascroscopic PK1 with respect to the design variable can be expressed as

$$\begin{aligned}\frac{\partial \boldsymbol{P}_{\mathrm{M}}}{\partial s_i} &= \frac{1}{|Y|}\int_{\mathcal{Y}_0}\frac{\partial \boldsymbol{P}_{\mathrm{m}}}{\partial s_i}\mathrm{d}Y \\ &= \frac{1}{|Y|}\int_{\mathcal{Y}_0}\eta s_i^{\eta-1}\left(\frac{\partial \Psi_2}{\partial \boldsymbol{F}_{\mathrm{m}}}-\frac{\partial \Psi_1}{\partial \boldsymbol{F}_{\mathrm{m}}}\right)\mathrm{d}Y \\ &= \frac{1}{|Y|}\int_{\mathcal{Y}_0}\eta s_i^{\eta-1}\left(\boldsymbol{P}_2-\boldsymbol{P}_1\right)\mathrm{d}Y, \end{aligned} \tag{30}$$

which can be evaluated, once the microscopic PK1 stresses $\boldsymbol{P}_1$ and $\boldsymbol{P}_2$ are obtained. Thus, the derivation of the sensitivity in this manner is worthy to be called the *two-scale sensitivity analysis*. Note here that the mathematical formulation of the two-scale adjoint sensitivity analysis mentioned above is carried out along the line of Nakshatrala et al. [23]. The main difference in the present sensitivity analysis is the procedure to evaluate $\boldsymbol{P}_1$ and $\boldsymbol{P}_2$ caused by the decoupling expression of micro- and macro BVPs. The influence of this difference is described in detail in section 4.2.

4.2. Summary and remarks

The procedure of this two-scale sensitivity analysis can be summarized as follows: In the equilibrium state at the final loading step of a macrostructural analysis, (i) apply the macroscopic displacement gradient $\tilde{\boldsymbol{H}}(\boldsymbol{X})\,(=\boldsymbol{F}_{\mathrm{M}}(\boldsymbol{X})-\boldsymbol{1})$ at each integration point of the macroscopic FE model to the unit cell as a datum in Equation (3) and solve the microscopic BVP; (ii) evaluate the microscopic PK1 stresses $\boldsymbol{P}_1$ and $\boldsymbol{P}_2$ at each integration point of the microscopic FE model, and (iii) use these values in Equation (30) to obtain the sensitivity $\partial \boldsymbol{P}_{\mathrm{M}}/\partial s_i$ in Equation (29).

As can be recognized in the procedure described here, to eventually obtain the sensitivity of the objective function in Equation (29), the two-scale sensitivity analysis needs to be conducted by way of the computational homogenization at all the integration points of the macroscopic FE model. This implies that the computational cost increases as the number of elements for the macroscopic model increases. It should be emphasized, however, that, owing the use of the decoupling multi-scale analysis scheme, the computational cost of the micro-macro concurrent topology optimization method proposed in this study is substantially less than those relying on the coupling scheme.

The final remark must be addressed on a defect due to the decoupling scheme. It is to be noted here that the microscopic equilibrated microscopic PK1 stresses in Equation (30) are the solutions of the microscopic BVP for the unit cell subjected to the macroscopic deformation gradient $\boldsymbol{F}_{\mathrm{M}}(\boldsymbol{X})=\tilde{\boldsymbol{H}}(\boldsymbol{X})+\boldsymbol{1}$, obtained as a solution of the macroscopic BVP at the final loading step. What matters here is the fact that the macroscopic PK1 stress $\boldsymbol{P}_{\mathrm{M}}$ in the left-hand side of Equation (30) is not consistent with the macroscopic PK1 stress used to attain the macroscopic equilibrium state in

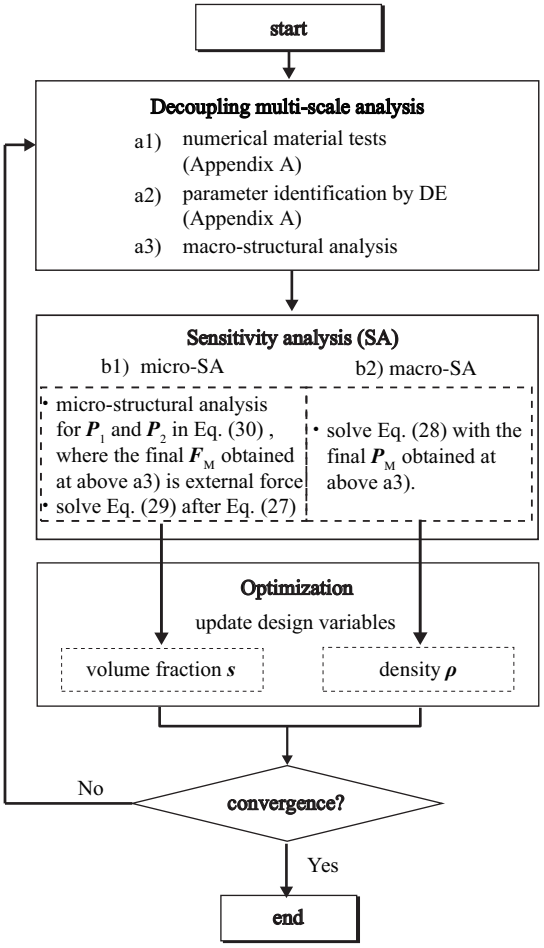

Figure 2. Flowchart of the proposed multi-scale optimization process.

Table I. Material parameters for Mooney-Rivlin model

	C_1	C_2	D
phase-1	1.923×10^2	0	1.6×10^{-3}
phase-2	1.923×10^3	0	1.6×10^{-4}

the decoupling multi-scale analyses. In other words, the macroscopic material behavior represented by the assumed macroscopic constitutive equation may not be able to represent the homogenized material response evaluated with Equation (5), which is consistent with the two-scale sensitivity derived above. Therefore, the concurrent multi-scale topology optimization proposed in this study crucially hinges on the reliability of the selected macroscopic constitutive equation as well as on the accuracy of parameter identification. This issue will be revisited and discussed when the performance of the proposed method is demonstrated in the numerical examples.

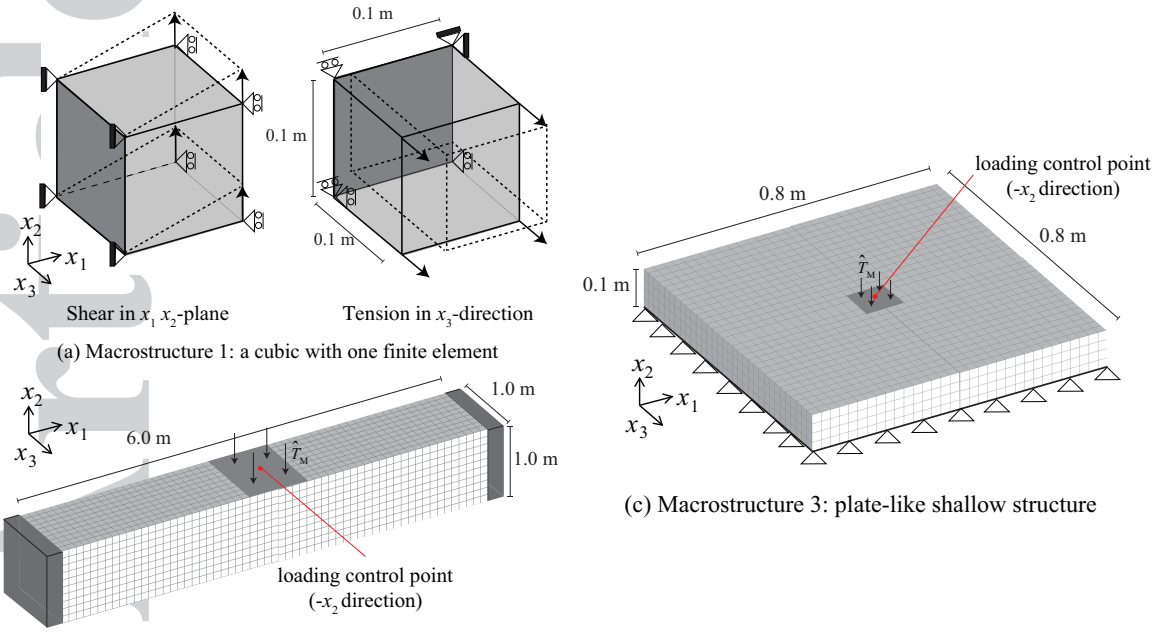

(a) Macrostructure 1: a cubic with one finite element

(b) Macrostructure 2: beam-like structure with both ends fixed

(c) Macrostructure 3: plate-like shallow structure

Figure 3. Macrostructures with support and loading conditions.

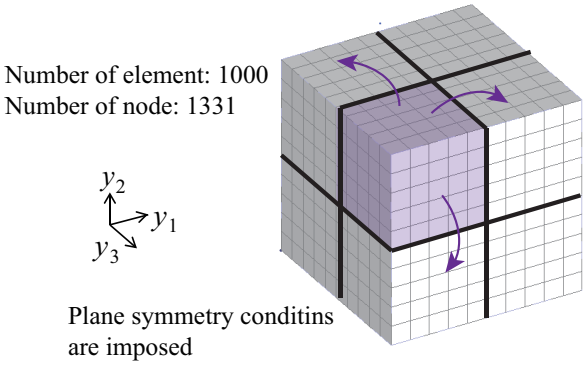

Figure 4. Unit cell's FE model with plane symmetry conditions.

5. PRELIMINARY VERIFICATION

5.1. Conditions for preliminary verification

This section illustrates simple optimization calculations to verify the performance of the proposed method before specific numerical examples presented in Section 6.

For the verification, we employ two macroscopic FE models, Macrostructure 1 and 2, as shown in Figure 3 (a) and (b), respectively. Macrostructure 1 is subjected to two-patterns of simple deformation modes; one is shear in the x_1x_2-plane and the other is tension in the x_3-direction. The reason for using such a simple macrostructure is to make the detailed examination and interpretation of the optimization results easy. Macrostructure 2 is a beam-like structure composed of multiple elements with both ends being fixed and subjected to transverse loading. In the preliminary

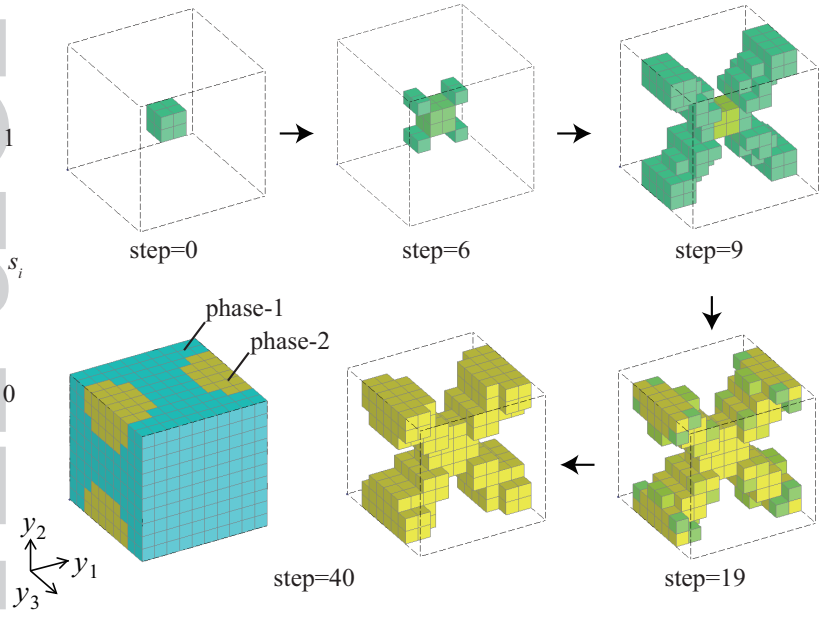

(a) Shear in x_1x_2-plane

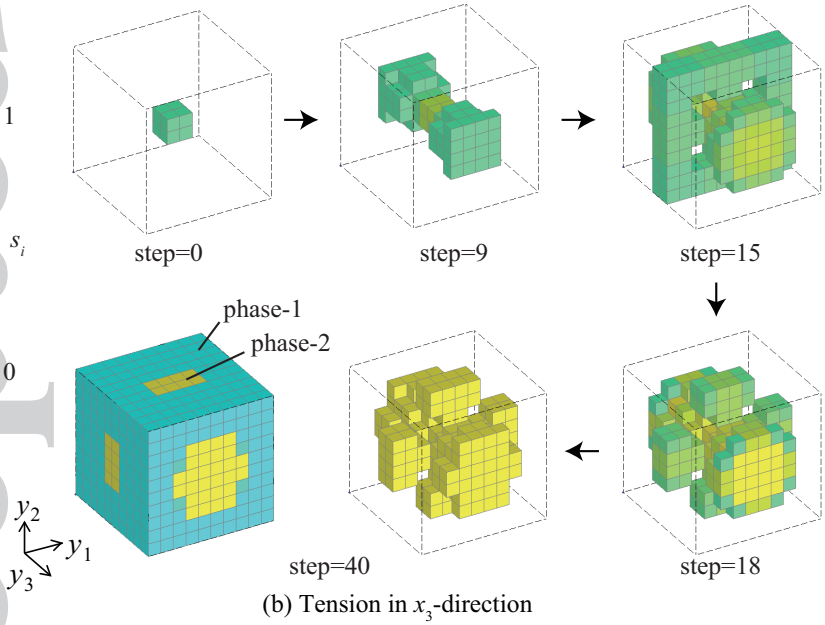

(b) Tension in x_3-direction

Figure 5. Transition of unit cell topology for Macrostructure 1.

verification with these models, the macroscopic topologies are not optimized to focus our attention only to the microscopic topology optimization, implying that all the macroscopic design variables are fixed at ρ (= 1.0) during optimization.

Meanwhile, the unit cell's FE model used for both of the macroscopic models is a cube with eight-node hexahedral elements as shown in Figure 4, which consists of two materials (phase-1 and phase-2). The entire unit cell region is used for microscopic analysis, while the one-eighth is used for optimization to reduce the computational costs as well as to impose plane symmetries with respect to

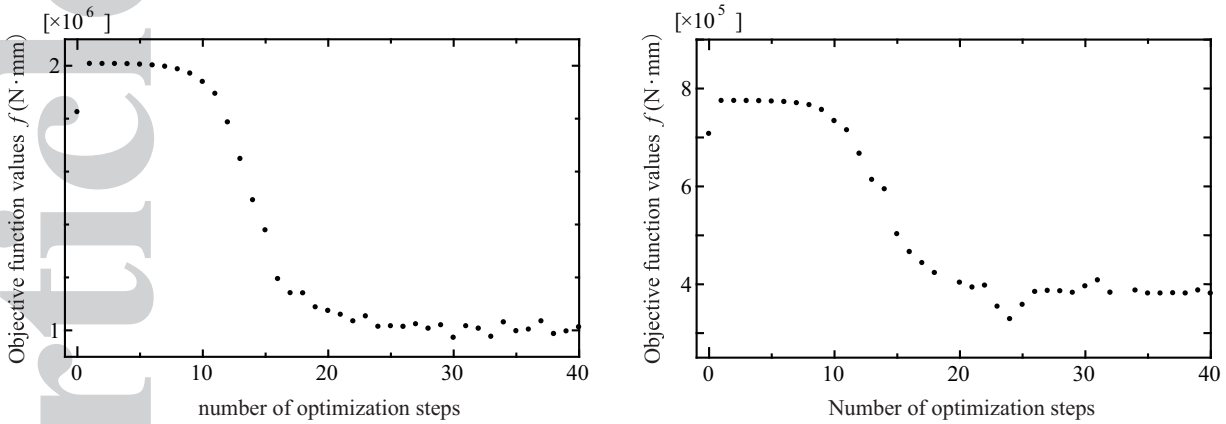

(a) Shear in x_1x_2-plane (b) Tension in x_3-direction

Figure 6. Optimization history of objective values for Macrostructure 1.

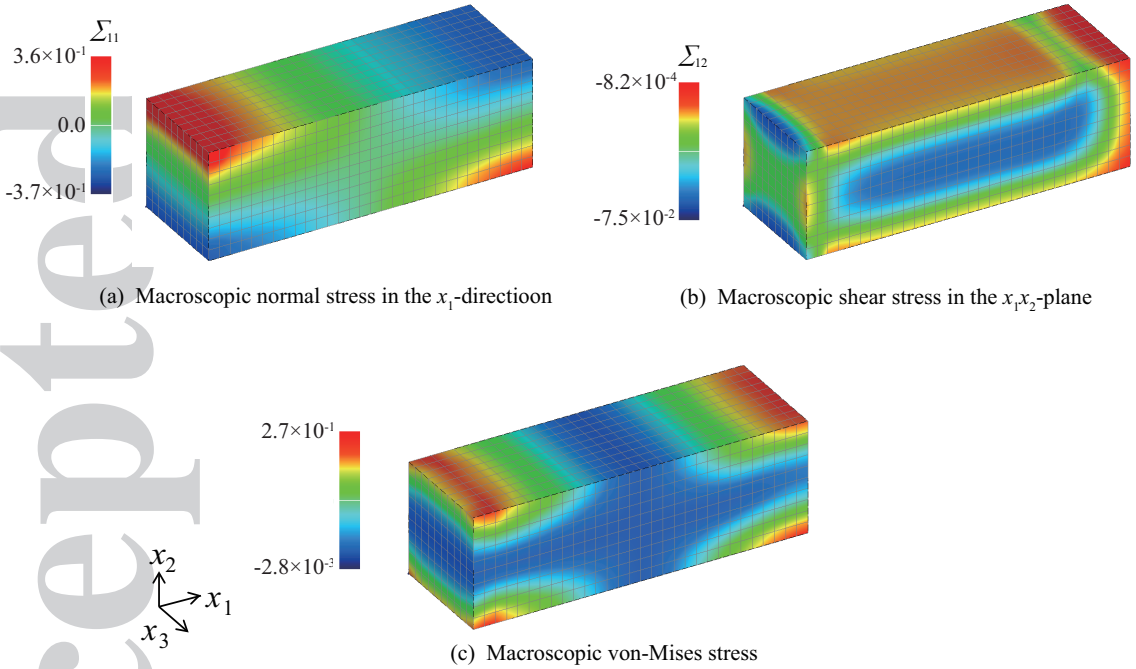

(a) Macroscopic normal stress in the x_1-directioon (b) Macroscopic shear stress in the x_1x_2-plane

(c) Macroscopic von-Mises stress

Figure 7. Macroscopic stress distributions in Macrostructure 2 (only the left half of the structure is displayed).

the three coordinate planes. The constraint on the material volume fraction of phase-2 in the unit cell is set to be 25% for both of the macrostructures and the same value is set as initial values of all the design variables in the unit cell model except for the element located at the center of the unit cell, to which a value 0.01 larger than the surrounding elements is assigned. This exception provides a slight excitation to avoid numerical instability. That is to say, if the same initial value is given to all the elements in the unit cell and if uniform macroscopic deformation is imposed on it, the microscopic stress/strain distribution will be the same over the unit cell, implying that the sensitivity $\partial f/\partial s_i$ does

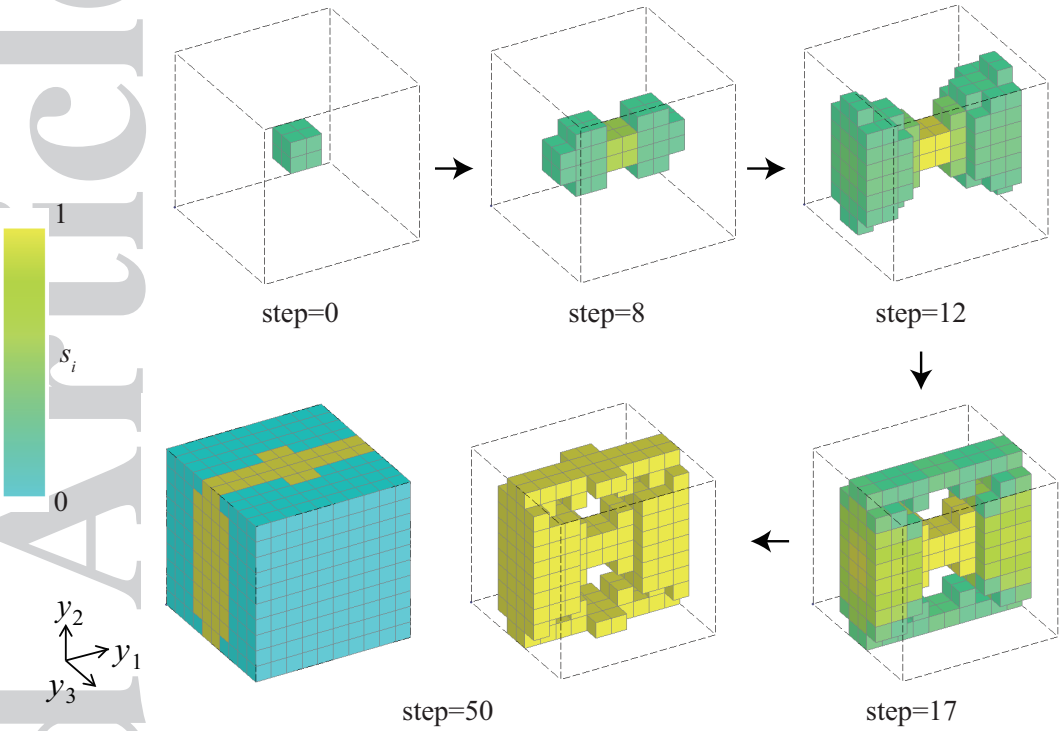

Figure 8. Transition of unit cell topology for Macrostructure 2.

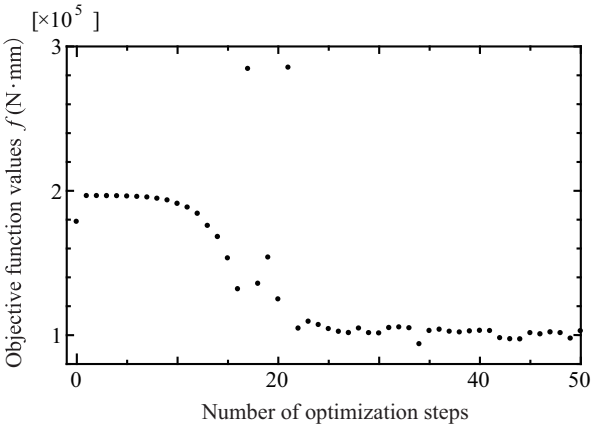

Figure 9. Optimization history of objective values for Macrostructure 2

not make sense to update the design variables. Also, to prevent the optimized topology from staying in a checkerboard layout, one of the mesh-independent filtering methods [38, 39] is adopted. The filter radius is set to initially be three times the element length in the unit cell and gradually reduced as the optimization step advances in order to obtain "0-1" clear separation. Moreover, to make the results easily understandable, the directions of the microscopic coordinate axes, y_1, y_2 and y_3 are set to correspond to the microscopic ones, x_1, x_2 and x_3, respectively.

The microscopic constitutive model assumed for the unit cell is the Mooney-Rivlin model, whose function form is presented in Appendix B, and the selected material constants are provided in Table I. The power of the interpolation function (8) is set at $\eta = 3$. According to the arguments on the method of decoupling multi-scale analysis described in Section 2, the Kaliske's material model is judged suitable for the macroscopic constitutive equation as it is recognized as an orthotropic version of the Mooney-Rivlin model. In this study, the method of differential evolution (DE) [32] is employed as an optimization algorithm to identify the material parameters of the selected macroscopic constitutive equation with the use of NMT results. The number of agents is 120 and the iteration number in DE is at most 50 for each case of this verification and also the numerical examples shown in the next section. Although there might be more efficient number of agents from viewpoints of accuracy of parameter identification and computational costs, this is not deeply investigated in this study.

5.2. Verification with Macrostructure 1

This section presents the results of optimization for Macrostructure 1, on which either shear or tensile deformation is imposed. Figure 5 shows how the topologies of the unit cells are optimized in response to these macroscopic deformations. Here, phase-2 is yellow-colored. To make the topological features inside the unit cells visible, only the design variables greater than or equal to 0.26 are depicted in the figure, as the material volume fraction of phase-2 is constrained to be 25%.

Figure 5(a) shows how the topologies during the optimization, starting from the central part to which a slight excitation is given, is formed in the diagonal direction to resist the macroscopic shear deformation. Figure 5(b), on the other hand, shows the transition of the microscopic topology, in which phase-2 evolves from the central part in the y_3-axis in accord with the macrosopic tensile direction. This evolution in the y_3-direction is followed by the material configuration to resist the shrinkage in the directions perpendicular to the macroscopic tensile direction due to Poisson's effect; see step =15 of Figure 5(b). Then the topology obtained at the final topology is reasonable enough from the mechanical viewpoints.

Figure 6 illustrates the histories of the values of the objective function, which gradually become smaller and stationary in both cases. The results demonstrate the validity of the unit cell topologies obtained by the proposed method. However, each of these transitions to the stationary state is unstable in some degree. This is partially due to the fact that the identification of the material parameters of the macroscopic constitutive equation occasionally fails. In fact, since the macroscopic stress is evaluated with the assumed macroscopic constitutive equation in the decoupling multi-scale analyses conducted during the optimization process, the equality (5) in the computational homogenization is not necessarily satisfied according the identification accuracy. In this sense, the reliability and robustness of the employed evolutionary optimization algorithm must be related to this instability problem. Also, the assumed macroscopic constitutive equation may not be able to represent the actual material behavior, which is supposed to be evaluated by microscopic analyses for unit cells in the micro-macro coupling scheme. This might be perceived as weakness of the present method based on the decoupling approach.

5.3. *Verification with Macrostructure 2*

As an extension, this subsection presents optimization of Macrostructure 2 shown in Figure 3, which is a beam-like structure composed of multiple elements with both ends being fixed. Considering the symmetry of the design domain, the left half of the macroscopic FE model is used for macroscopic analysis.

Figure 7 shows the distributions of some macrostructural stress measures at the final loading step. Here, the macroscopic Cauchy stress $\boldsymbol{\Sigma}$ is calculated from the macroscopic PK1 stress $\boldsymbol{P}_{\mathrm{M}}$ (or $\bar{\boldsymbol{P}}_{\mathrm{M}}$) as

$$\boldsymbol{\Sigma} = \frac{1}{J_{\mathrm{M}}} \boldsymbol{P}_{\mathrm{M}} \boldsymbol{F}_{\mathrm{M}}^{\mathrm{T}}, \tag{31}$$

where $J_{\mathrm{M}} = \det \boldsymbol{F}_{\mathrm{M}}$ is the Jacobian of the macroscopic deformation gradient. It can be seen from the figure that the normal stress Σ_{11} is dominant and the shear stress Σ_{12} is broadly distributed. Note that the stress within the unit cell could be much greater than the macro-stress $\boldsymbol{\Sigma}$ since $\boldsymbol{\Sigma}$ is averaged over the unit cell. This is a common recognition in homogenization theory.

Figure 8 shows the unit cell's topologies obtained in some optimization steps. It can be seen from this figure that, reflecting the macroscopic stress distributions shown above, phase-2 is first formed to reinforce the macrostructure in the y_1-direction and then the reinforcement against the shear stress in the y_1y_2-plane is obtained. The corresponding history of the objective function value is drawn in Figure 9, which exhibits a deceasing trend, implying that a substantial reduction of the amount of macroscopic deformation can be expected. Thus, it has been demonstrated that an effective microscopic topology can be obtained by the proposed optimization method.

However, as can be seen from Figure 9, the objective function values at the 17th and 21st optimization steps became oddly large. Again, this is probably due to the inappropriate identification of the material parameters of the macroscopic constitutive equation, as discussed above. That is, this kind of instability possibly occurs, when the identification cannot be assured. In the present study, when – based on the obtained values of the objective function – it is judged that apparently inappropriate parameters have been identified, we return to the previous optimization step and conduct parameter identification again before moving on to the subsequent optimization steps.

In summary, it is confirmed that the present method of topology optimization for unit cells is a practical approach mostly capable of reaching the optimal solution, though the plausibility partially depends on the accuracy of parameter identification. Needless to say, however, to find the reliable and appropriate macroscopic constitutive equation is of paramount importance.

6. NUMERICAL EXAMPLES

This section presents specific optimization calculations to conduct the verification and demonstrate the capability of the concurrent multi-scale topology optimization proposed in this study.

6.1. *Calculation conditions*

We utilize two macroscopic FE models provided in Figures 3(b) and (c), which are referred to as Macrostructures 2 and 3, respectively. For both of the macrostructures, the material volume fraction is set at 20% and the initial value of macroscopic design variable is set as $\rho_I = 0.2$ for

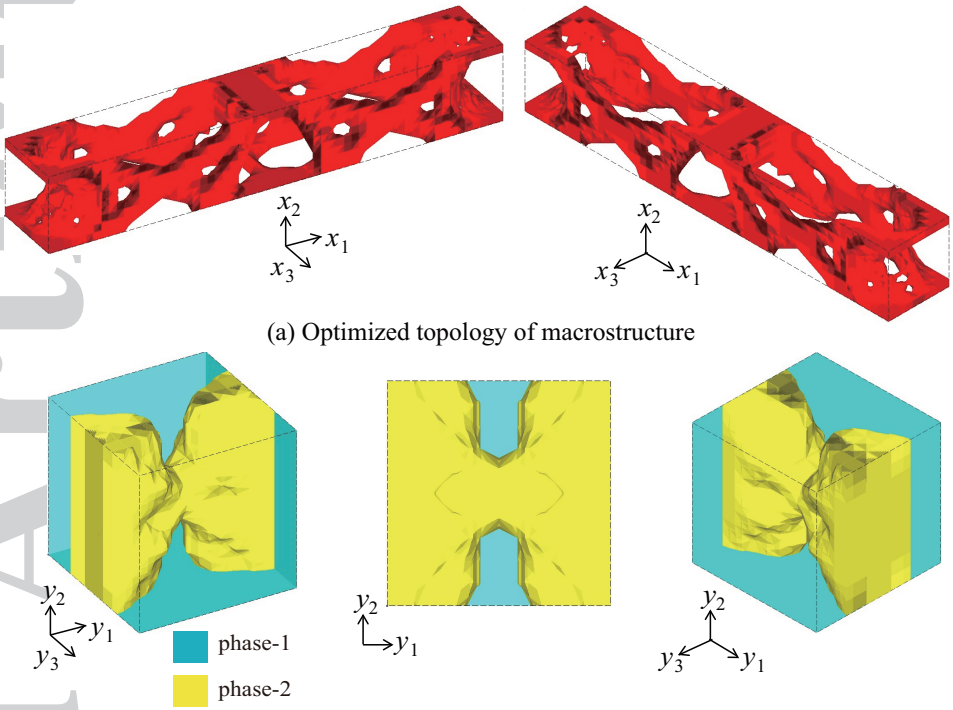

(a) Optimized topology of macrostructure

(b) Optimized topology of microstructure

Figure 10. Optimization results for Macrostructure 2 with the microstructure (beam-like structure with both ends being fixed) subjected to a low-level load.

all the elements. For the materials in the unit cell model, the same set of material properties and the power η are used as in the previous section. The volume fraction of phase-2 is set to be 25% for Macrostructure 2 and 30% for Macrostructure 3. These volume fractions are given as initial values of the design variables to the elements in the macroscopic FE model except for the elements in the central region of the unit cell.

To carry out nonlinear macroscopic analyses during the optimization process, an incremental load-controlled scheme is employed. To this end, the macroscopic FE equilibrium equation (14), which can be re-written as

$$\boldsymbol{R}_{\mathrm{M}} = \boldsymbol{F}_{\mathrm{int}} - \gamma \boldsymbol{F}_{\mathrm{ext}} = \boldsymbol{0}, \tag{32}$$

which is to be solved with the load factor γ being gradually increased. Here, $\boldsymbol{F}_{\mathrm{ext}}$ involves the referential macroscopic traction force $\hat{\boldsymbol{T}}^0_{\mathrm{M}}$ as in (17), but is assumed not to have body forces. In this study, $\hat{\boldsymbol{T}}^0_{\mathrm{M}}$ is fixed at 1.0 (N/mm^2)

Remember that the present method has been developed for largely deforming solids. Therefore, the optimized topologies are expected to be different according to the load levels applied at the boundary, even though the hyperelastic material models, which are path-independent, are used. To examine this capability, two different load levels, controlled by the load factor γ, are set in the numerical examples below.

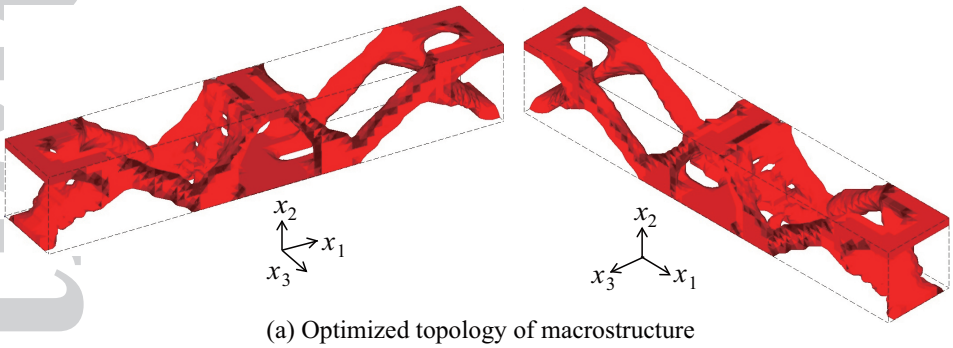

(a) Optimized topology of macrostructure

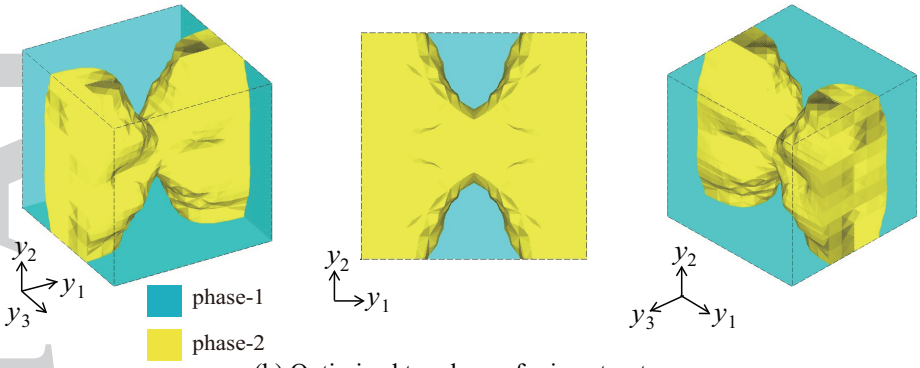

(b) Optimized topology of microstructure

Figure 11. Optimization results for Macrostructure 2 with the microstructure (beam-like structure with both ends being fixed) subjected to a high-level load.

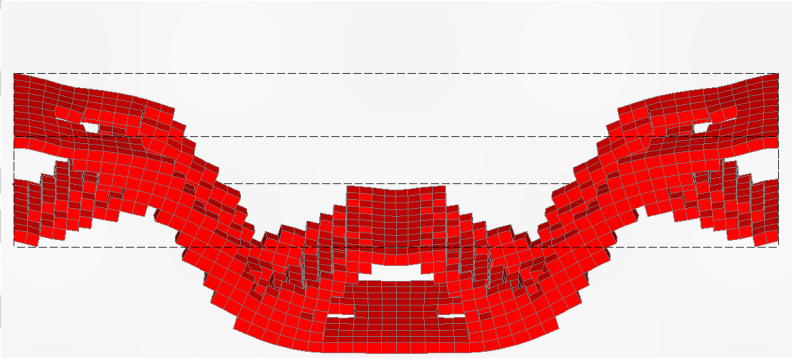

Figure 12. Deformation of the optimized Macrostructure 2 with unscaled finite element mesh subjected to a high-level load.

6.2. Micro-macro concurrent topology optimization with Macrostructure 2

Using Macrostructure 2 under the given boundary conditions, we conduct two optimization calculations to demonstrate the capability of the proposed method for micro-macro concurrent topology optimization: one is with $\gamma = 1.0 \times 10^{-6}$ and the other with $\gamma = 0.1$ for relatively low- and high-level loads, respectively. The optimization results with both of the conditions are shown in Figures 10 and 11, which can be recognized as optimized topologies. Figure 12 also displays the deformed geometry of the optimized Macrostructure 2 with unscaled finite element mesh for the high-level load, from which one can understand the degree of geometrical nonlinearity, and

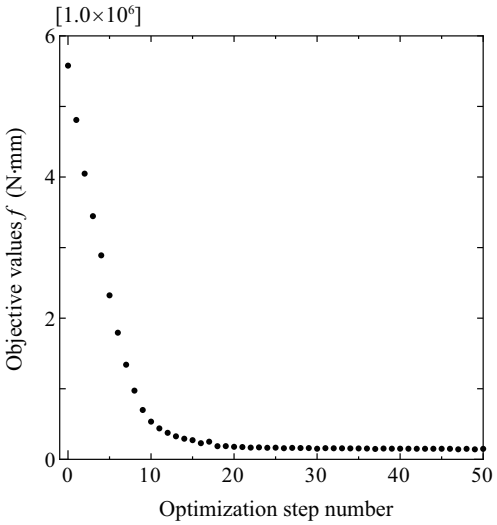

Figure 13. Optimization history of Macrostructure 2 (beam-like structure with both ends being fixed) subjected to a high-level load.

the corresponding history of the objective function provided in Figure 13 exhibits a monotonically decreasing trend.

Looking at the optimized macroscopic topology in Figure 10, which is obtained with a low-level load, we can see that it is similar to a standard truss structure that is subjected to bending about x_3-axis. In Figure 11, on the other hand, the obtained macroscopic topology clearly features a thick diagonal member in the middle portion between the center and the fixed end of the beam. In fact, the macroscopic membrane force becomes dominant as the external load increases. This results in the tendency to obtain the topologies of a suspended structure that diminish the elongation in the longitudinal direction rather than the bending deformation. The same tendency, which is reasonable from the mechanical viewpoint, is also realized by Buhl et al. [40] and Matsui et al. [41] within the two-dimensional context.

Keeping in mind that the macrostructure is formed to resist tensile/compressive deformation in the longitudinal x_1-direction and the x_1x_2-plane shear deformation, we now focus on the optimized topology of the unit cell (periodic microstructure) shown in Figure 10. It can be seen from the figure, phase-2 (yellow-colored) in the obtained microscopic topology, which is relatively stiff, is largely resistant to both longitudinal deformation in the y_1-direction and shear deformation on the y_1y_2-plane. Also, phase-1 (blue-colored), which is relatively soft, is located only to keep the continuity in the y_3-direction, to which the unit cell needs no resistance. Thus, it may be safe to conclude that the obtained topology of the unit cell is reasonable enough from the mechanical viewpoint to reflect the macroscopic structural behavior. Although such a rough consideration is possible, it seems to be difficult to further clarify the mechanical implications of the obtained microscopic topology in a strict sense.

When a high-level load is applied, the optimized topology of the unit cell is obtained as shown in Figure 11. The obtained topology is very similar to that obtained for a low-level load shown in Figure 10, though there are slight differences especially in the y_1y_2 front view. This is probably

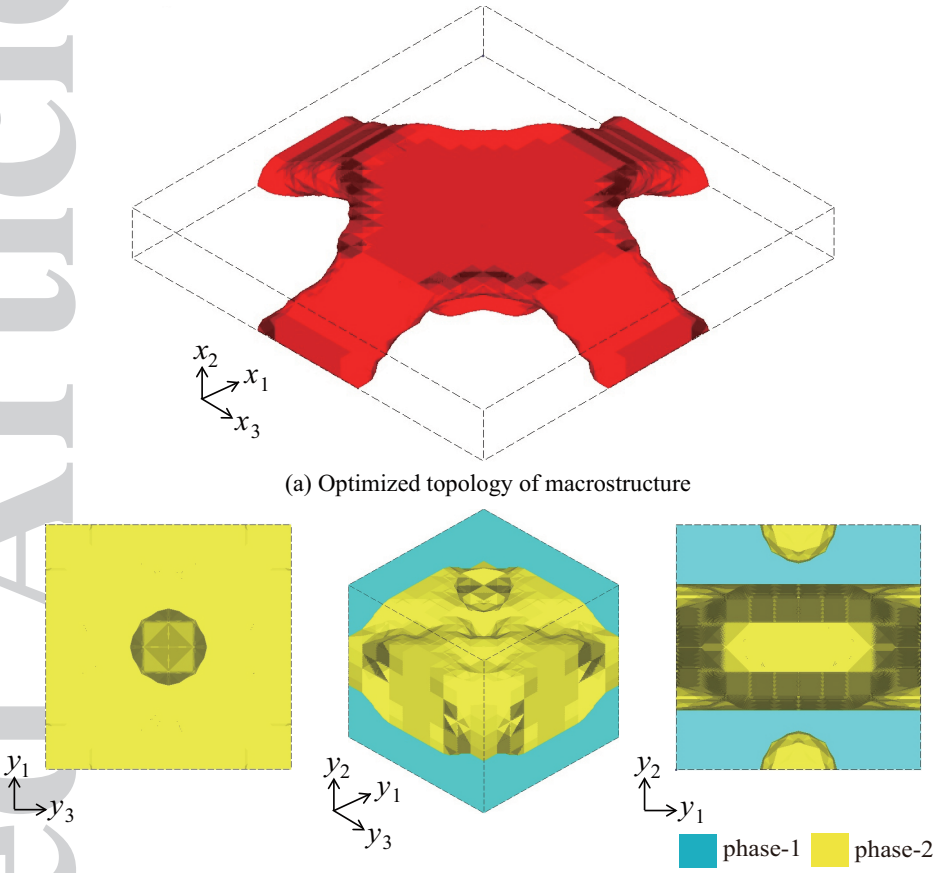

(a) Optimized topology of macrostructure

(b) Optimized topology of microstructure

Figure 14. Optimization results for Macrostructure 3 with the microstructure (plate-like shallow structure) subjected to a low-level load (Case-L).

due to the fact that there is little difference in the direction of the dominant macroscopic stress component, regardless of the increase in the amount of deformation. Even if a much larger load is applied, the situation cannot drastically change, as a slender structure is commonly expected to possess the load bearing capacity in the longitudinal stiffness.

However, excessively high loads often provoke another problem inherent to finite deformation problems. That is, when the macrostructure is severely deformed, the determinants of the deformation gradients, J_{M}, at some integration points likely become negative, making it impossible to further advance the macroscopic calculation. The situation is caused by the extremely low resistance of a low-density material assigned at those points. This is a well-known headache to topology optimization problems in consideration of finite deformations, for which some countermeasures have been proposed [42, 43]. The present study, however, has employed none of them. Even effective countermeasures easily make the main optimization problem unnecessarily complex, but some of them might be worthy of attention in future studies.

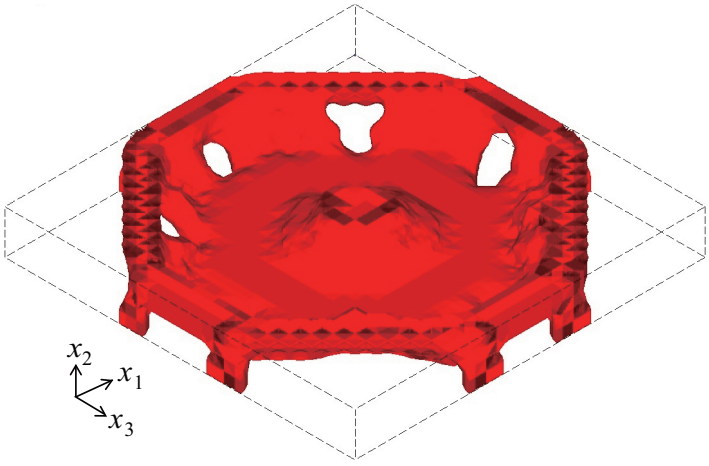

(a) Optimized topology of macrostructure

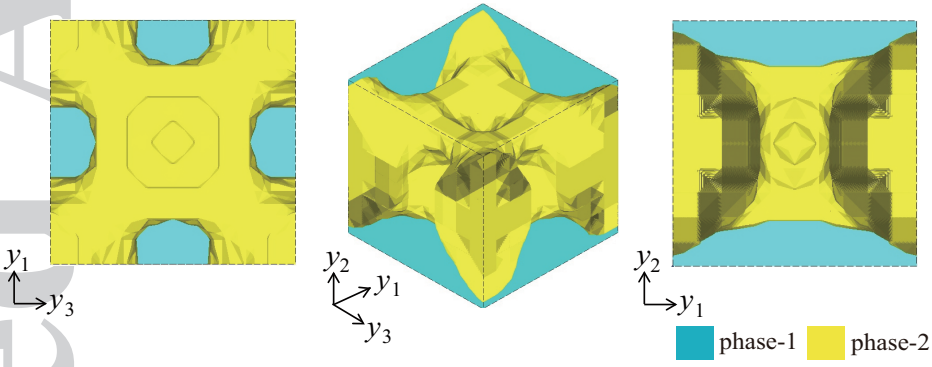

(b) Optimized topology of microstructure

Figure 15. Optimization results for Macrostructure 3 with the microstructure (plate-like shallow structure) subjected to a high-level load (Case-H).

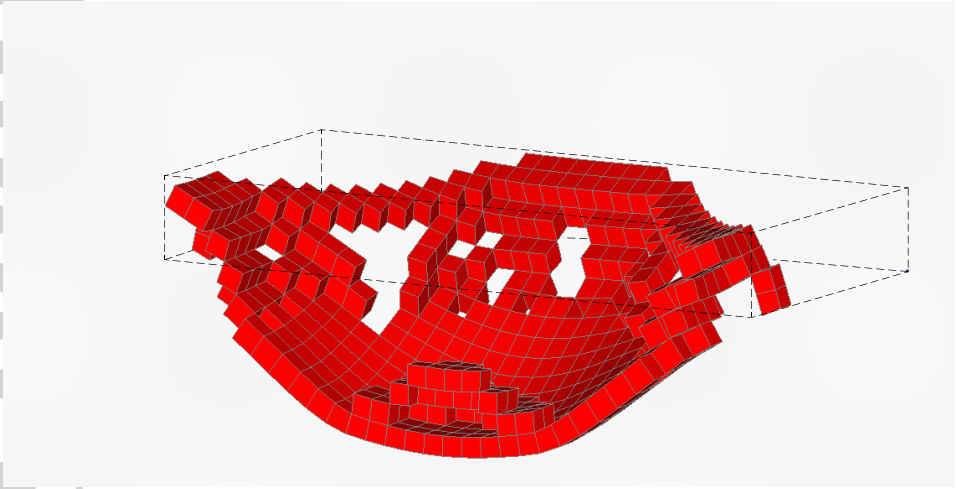

Figure 16. Deformation of the optimized Macrostructure 3 (only half structure is displayed with unscaled finite element mesh) subjected to a high-level load.

6.3. Micro-macro concurrent topology optimization with Macrostructure 3

A numerical example with the plate-like shallow structure shown in Figure 3(c) is presented here. As in the previous subection, two different levels of uniformly distributed loads are considered. We set $\hat{\boldsymbol{T}}_{\mathrm{M}} = 0.1$ (N/mm^2) for the case of lower-level loading (Case-L) and $\hat{\boldsymbol{T}}_{\mathrm{M}} = 2.5$ (N/mm^2) for the case of higher-level loading (Case-H), with the aim of realizing different topologies of both the unit cells and macrostructures. The load factors corresponding to these load levels are $\gamma = 0.1$ and $\gamma = 2.5$, respectively.

First, let us look at the macroscopic optimized topologies. Figures 14(a) shows the obtained macroscopic topology for Case-L. As can be seen, the macroscopic topology is in the shape of a cross, which is named as *cross-figure topology*, and its legs are formed in the macroscopic principal directions that are in accordance with the x_1 and x_3-directions. At the same time, the cross-sectional shape of this macroscopic topology reveals a material layout like an arch-shaped truss structure, which is typically obtained in minimizing the compliance of a simply-supported beam-like design domain within the small strain framework. Thus, it is probably safe to say that the minimization of the macroscopic end compliance is equivalent to the maximization problem of the stiffness of a linearly elastic body within the range of sufficiently small deformation.

On the other hand, large deformation of the macrostructure is expected for Case-H and leads to the optimized macroscopic topology shown in Figure 15 (a), which is totally different from that of Case-L; that is, they are upside down. Figure 16 also displays the deformation of the half of the optimized Macrostructure 3 for Case-H with unscaled finite element mesh. In fact, the macroscopic topology obtained here exhibits a bowl-like structure whose side surfaces are suspended to resist the in-plane or membrane force and whose center portion forms a bell-shaped base to support the external load. It follows from what has been examined here that the minimization of end compliance in the present method adequately provided optimized macroscopic topologies according to the amount of deformation.

Here, in order to understand the mechanical implications of the optimization results more in detail, we compare the above results with those obtained by Kemmler and Ramm [44], who conducted the topology optimization of a rectangular thin plate structure subjected to similar loading and support conditions within finite deformation and single-scale frameworks. In their study, the end compliance is employed as an objective function and an isotropic material interpolation scheme, SIMP method, is utilized. Their expected optimal topology in the case of small deformation is a *cross-figure* one, similar to Figure 14(a), whose principal axes are directed to the short axes of the rectangular design domain. In contrast, the principal axes of the optimized topology are directed to the diagonals of the rectangular design domain in the case of large deformation. Since the end compliance minimization is aimed at increasing the stiffness in the final state of deformation, their results are reasonable enough from the mechanical viewpoints. In fact, the diagonals, which have longer spans than the edges of the rectangular domain, are advantageous to suppress the deflection with the same material volume. However, this remarkable finding associated with geometrical nonlinearity seems not to be consistent with the above discussions about our macroscopic optimization results, which were obtained within the two-scale framework. The important point to note in this context might be that the present multi-scale topology optimization

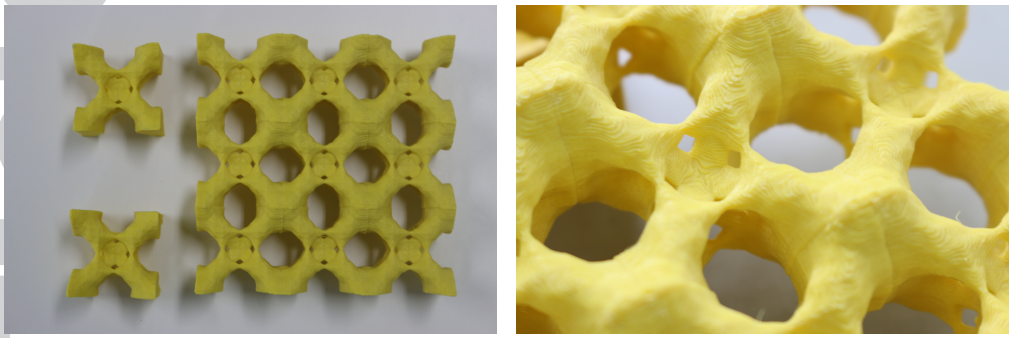

(a) View from y_1y_3–plane of multiply-arranged optimized unit cells

(b) Zoom of (a)

Figure 17. 3D printer outputs of optimized unit cells obtained for Case-H with Macrostructure 2 subjected to a high-level of loading: the diagonal direction of the microstructure corresponds with that of the macrostructure

enjoys anisotropy in the macroscopic elastic property when producing the effect of geometrical nonlinearity.

Next, to deepen the debate on the effect of geometrical nonlinearity, let us focus our eyes on the optimized microscopic topologies in Figures 14 and 15. They are actually quite different according to the load levels, though, as a whole, the stiffer material (phase-2) in both of them are formed in a planar shape in the y_1y_3-plane to resist the macroscopic in-plane (x_1x_3) stress, which is indeed dominant in the macrostructure. More specifically, it can be recognized that the macroscopic elastic property characterized by the microstructure shown in Figure 14(b) is mostly isotropic in the y_1y_3 plane, while that in Figure 15(b) reveals orthotropy in the direction inclined at 45 degrees with respect to the y_1 and y_3 axes.

To clearly study the three-dimensional material layout of the microscopic optimization result illustrated in Figure 15, we present in Figure 17 a 3D printer output of the optimized topology consisting of $3 \times 3 \times 1$ unit cells. In this output, the phase-1 portions (blue-colored) are removed and only the phase-2 part (yellow-colored) is created to make it clearer. It is evidently recognized that phase-2 is distributed in the direction diagonal to the y_1 and y_3 axes of the microstructure.

In view of the above discussions, it must be interesting to compare the micro- and macroscopic optimized topologies for Case-H again with the result reported in [44], which addresses the topology optimization of a thin plate with an isotropic material. As mentioned above, each of the main axes of the optimized "macroscopic" topology in [44] shifts to the diagonal of the rectangular domain in response to an increase in the amount of deformation. In contrast, the optimized macroscopic topology seems not to have preferred directions, while the optimized "microscopic" topology obtained in the present study exhibits orthotropy in its macroscopic elastic property as pointed out before. This is highly suggestive of the capability of the proposed method of concurrent multi-scale topology optimization in creating products whose micro-macro structures together fulfill the preferable functions.

In summary, the concurrent multi-scale topology optimization proposed in this study is a practically useful and versatile approach, capable of obtaining mechanically reasonable optimal structures at both micro- and macro-scales, according to the levels of applied loads.

7. CONCLUSIONS

With the aim of simultaneously optimizing the topologies of micro- and macrostructures of 3D two-phase nonlinear solids undergoing large deformation, we developed a method of concurrent multi-scale topology optimization that embeds the decoupling multi-scale analysis scheme for computational homogenization. While the standard SIMP method was employed for the macroscopic optimization problem, the microscopic optimization problem adopted the SIMP-like method, which replaces the set of "void" and "solid" in the original SIMP by two separate solid materials, to interpolate the effective microscopic stress. The macroscopic end compliance was taken as an objective function to be minimized and hence the two-scale sensitivity analysis presented in this study must be conducted only for the final state of equilibrated micro- and macrostructures under a certain level of loading. Then the addressed two-scale optimization problem was split into micro- and macroscopic one for algorithmic simplicity. After two preliminary verifications were conducted, two sets of numerical examples with different levels of applied loading were presented to demonstrate the capability of the proposed method. In particular, the actual optimization calculations provided separate topologies of micro- and macrostructures according to the applied load levels, which are reasonable from the mechanical viewpoints, exemplifying its validity and high performance.

Since the macroscopic constitutive equation, which is assumed with reference to the constitutive equations employed at the micro-scale, is used to evaluate the macroscopic stress in the decoupling scheme, the proposed method enables us to solve the two-scale BVP with reasonable computational costs. Although a hyperelastic composite is assumed in the formulation of the two-scale topology optimization, the framework of the proposed method accommodates a broad class of nonlinear solids such as elastoplastic materials. However, the success to the optimization hinges crucially on whether or not an appropriate macroscopic constitutive equation is found and its material parameters are properly identified. Thus, the proposed method is versatile to some extent, though not infallible.

Special attention must be drawn to the two-scale sensitivity with the decoupling scheme. Although the sensitivity of the macroscopic stress with respect to the design variable is evaluated with the use of the microscopic equilibrated stresses in the unit cell, the macroscopic stress used there is not necessarily the same as the one obtained with the assumed macroscopic constitutive equation in the decoupling scheme. Therefore, there is a possibility that the convergence behavior of a multi-scale concurrent optimization process may not be stable, as the accuracy of the sensitivity of the objective function is affected by the degree of conformity between those two macroscopic stresses with different origins. In this regard, the applicability to any type of nonlinearities may be questioned, though the framework posed in this study is general. Thus, it remains a challenge for future research to work with the decoupling multi-scale method along with a variety of inelastic material models at the micro-scale.

ACKNOWLEDGEMENT

This work was supported by MEXT KAKENHI Grant Numbers 16H04394 and 26630209. This support is gratefully acknowledged.

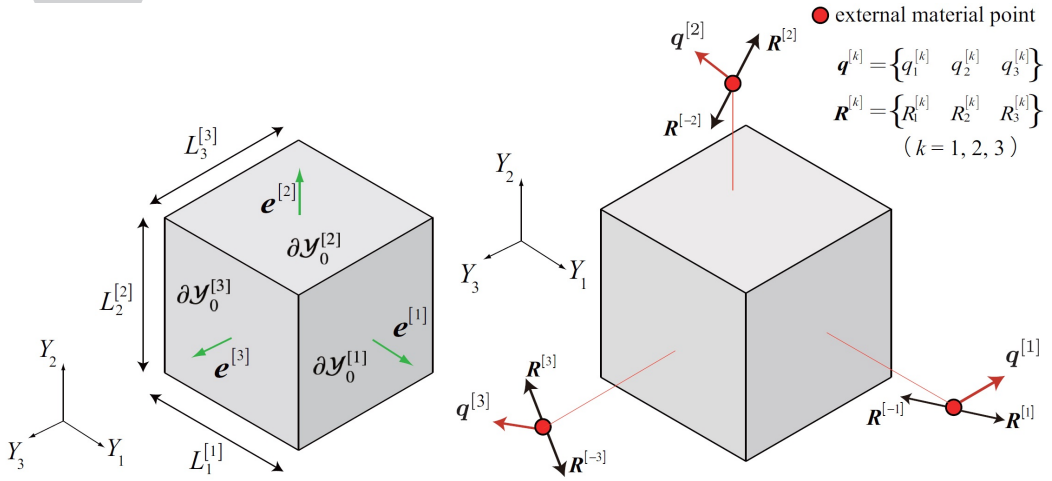

(a) Definitions of edges, surfaces and basis vectors in the microscopic coordinate system (b) External material points, to which either relative displacement or external force is prescribed

Figure 18. Unit cell equipped with external material points

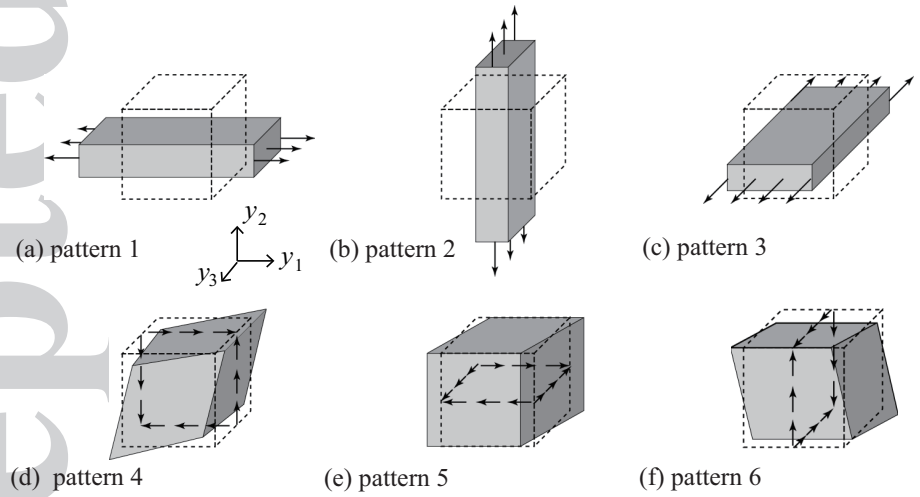

Figure 19. Deformation patterns of unit cells: (a) tension in the y_1-direction; (b) tension in the y_2-direction; (c) tension in they_3-direction; (d) shear in the y_1y_2-plane; (e) shear in the y_3y_1-plane; (f) shear in the y_2y_3-plane.

A. HOMOGENIZATION WITH NUMERICAL MATERIAL TESTING

This appendix is devoted to complementing the explanations made in Section 2. To describe the process of computational homogenization, we introduce the external material points for numerical material testing, and then explain how to determine the material parameters of an assumed macroscopic constitutive equation.

A.1. External material points

In order to solve the microscopic BVP effectively, we introduce external material points outside the unit cell domain, as shown in Figure 18(b), which is just a mass point in the finite element (FE) context. To understand the role of these points, let us re-write Equation (3), which corresponds to the periodic boundary conditions, by

$$\boldsymbol{w}^{[k]} - \boldsymbol{w}^{[-k]} = \boldsymbol{q}^{[k]}, \tag{33}$$

where $\boldsymbol{q}^{[k]} = \tilde{\boldsymbol{H}} \cdot \boldsymbol{L}^{[k]}$. Since $\boldsymbol{w}^{[\pm k]}$ are discretized with nodal displacements on a pair of facing or opposite boundary surfaces $\partial \mathcal{Y}_0^{[\pm k]}$ in the initial configuration, the left-hand side of Equation (33) yields pairs of relative (nodal) displacements between those surfaces. Inevitably therefore, each component of $\boldsymbol{q}^{[k]}$ has a degree of freedom of the relative displacement between two nodes located on the opposite sides. Thus, Equation (33) is regarded as a set of multiple point constraint (MPC) conditions after the FE discretization.

If all the components of $q_i^{[k]}$ are given on the external material point associated with a pair of boundary surfaces $\partial \mathcal{Y}_0^{[\pm k]}$, the components of reaction force vector $R_i^{[k]}$ on it correspond to the surface integral values of the components of microscopic traction force vector $t_{\mathrm{m}i}^{[k]}$ on the boundary surface $\partial \mathcal{Y}_0{}^{[k]}$. In short, this reaction force vector can be expressed as:

$$R_i^{[k]} = \int_{\partial \mathcal{Y}_0{}^{[k]}} t_{\mathrm{m}i}^{[k]} \mathrm{d}s. \tag{34}$$

Then, the ki-components of the macroscopic PK1 stress $P_{\mathrm{M}i}^{[k]}$ can be computed from this reaction force vector divided by the surface area $\left|\partial Y^{[k]}\right|$ of the unit cell boundary surface in the initial configuration.

It is to be noted that $q_i^{[k]}$ in Equation (33) can be either known or unknown component of relative displacement vector. That is, if specific value of $q_i^{[k]}$ is prescribed, implying that the macroscopic displacement gradient $\tilde{\boldsymbol{H}}$ is determined, $R_i^{[k]}$ is unknown. On the other hand, specific value of $R_i^{[k]}$, or equivalently $P_{\mathrm{M}i}^{[k]}$, is prescribed, $q_i^{[k]}$ is unknown.

A.2. Numerical material testing and parameter identification

In the decoupling multiscale analysis, a macroscopic material constitutive equation is assumed beforehand. To proceed to the macroscopic analysis , its material parameters have to be determined so as to properly represent the actual material behavior characterized by the heterogeneity in a unit cell. For that purpose, we carry out a series of numerical material tests (NMTs) to obtain 'empirical' data of the relationship between the macroscopic stresses and strains.

The data taken from the series of NMTs must contain enough information about the macroscopic material behavior. Therefore, at least six patterns of macroscopic deformation, shown in Figure 19, are usually considered to obtain the corresponding macroscopic stress responses along the lines of the linear homogenization process. For example, the input data, i.e., the macroscopic displacement

gradient $\tilde{\boldsymbol{H}}$ in Equation (33), corresponding to these patterns, are given in order as follows:

$$\text{(a) } \tilde{\boldsymbol{H}} = \begin{bmatrix} \hat{H}_{11} & 0 & 0 \\ 0 & * & 0 \\ 0 & 0 & * \end{bmatrix}, \quad \text{(b) } \tilde{\boldsymbol{H}} = \begin{bmatrix} * & 0 & 0 \\ 0 & \hat{H}_{22} & 0 \\ 0 & 0 & * \end{bmatrix}, \quad \text{(c) } \tilde{\boldsymbol{H}} = \begin{bmatrix} * & 0 & 0 \\ 0 & * & 0 \\ 0 & 0 & \hat{H}_{33} \end{bmatrix} \tag{35}$$

$$\text{(d) } \tilde{\boldsymbol{H}} = \begin{bmatrix} 0 & \hat{H}_{12} & 0 \\ \hat{H}_{12} & 0 & 0 \\ 0 & 0 & 0 \end{bmatrix}, \quad \text{(e) } \tilde{\boldsymbol{H}} = \begin{bmatrix} 0 & 0 & \hat{H}_{13} \\ 0 & 0 & 0 \\ \hat{H}_{13} & 0 & 0 \end{bmatrix}, \quad \text{(f) } \tilde{\boldsymbol{H}} = \begin{bmatrix} 0 & 0 & 0 \\ 0 & 0 & \hat{H}_{23} \\ 0 & \hat{H}_{23} & 0 \end{bmatrix} \tag{36}$$

Here, $\hat{H}_{ij}$ represents the specific component of the macroscopic displacement gradient to control the relative displacement in Equation (33), while * indicates that the corresponding component is unknown and cannot be controlled. Also, 0 indicates that the relative displacement between the boundary surfaces $\partial\mathcal{Y}_0^{[\pm k]}$ is fixed at zero throughout the microscopic analysis.

Once relationships between macroscopic stresses and strains are 'empirically' obtained by a series of NMTs, the material parameters of the assumed macroscopic constitutive equation can be identified by a certain optimization scheme. As mentioned in Section 2.2, the present study employs the differential evolution (DE) method [32], which is known as a high-performance optimization algorithm in terms of calculation speed and accuracy. To conduct DE for parameter identification, it is necessary to define appropriate vector populations and evaluation function. Each vector population is a candidate of the solution for the optimization problem prepared within a feasible domain, which is a vector having all design variables as components. In DE, an optimal solution is sought by updating the vector populations in accordance with a certain specified rule. On the other hand, an evaluation function indicates the goodness of fit of each vector population, and determines both superiority and inferiority among all the vector populations, enabling us to obtain the best vector population as the optimal solution.

The 'goodness of fit' evaluated by an evaluation function is measured by a certain definition of difference between 'empirical' data obtained by NMTs and the material responses obtained by the assumed macroscopic constitutive equation endowed with the material parameters identified with DE. In this study, the following evaluation function ϕ is employed to evaluate the difference, i.e., the identification accuracy:

$$\phi = \sum_{l=1}^{6} \phi^{[l]}, \tag{37}$$

where

$$\phi^{[l]} = \frac{1}{n_{\text{step}}} \sqrt{\sum_{i=1}^{n_{\text{step}}} \left({}^{i}S_{IJ}^{[l]} - {}^{i}\hat{S}_{IJ}^{[l]} \right)^2}. \tag{38}$$

Here, ${}^{i}\hat{S}_{IJ}^{[l]}$ indicates the IJ component of the macroscopic 2nd Piola-Kirchhoff (PK2) stress computed in the i-th load step in the NMT for deformation pattern l, while ${}^{i}S_{IJ}^{[l]}$ is that computed by the assumed macroscopic constitutive equation. Also, n_{step} represents the total number of load steps. In DE, an optimal solution is searched by minimizing this evaluation function, yielding the macroscopic material parameters that can simulate responses equivalent to those of numerical material testing as the optimal solution.

When DE is applied to identify material parameters of assumed macroscopic constitutive equation in actual decoupling multiscale analyses, the dimension of a vector population is equal to the number of the parameters to be determined. For example, when the anisotropic hyperelastic constitutive equation presented in Appendix B, the number of material parameters to be identified is 36 in total so that the vector population should be a vector of a maximum of 36 components; D in Equation (41), factors a_i to g_o in Equation (49) and the components of the unit vectors $\boldsymbol{A}$ and $\boldsymbol{B}$ indicating the fiber directions.

B. ISOTROPIC HYPERELASTIC CONSTITUTIVE LAW AND ITS ANISOTROPIC VERSION

The elastic potential of an isotropic hyperelastic body can be generally decomposed into the volume and isochoric parts, W_{vol} and W_{iso}, as

$$\Psi = \Psi(\boldsymbol{C}) = W_{\text{vol}}(J) + W_{\text{iso}}\left(\bar{\boldsymbol{C}}\right), \tag{39}$$

where $\boldsymbol{C}$ $(= \boldsymbol{F}^T\boldsymbol{F})$ is the right Cauchy-Green tensor with $\boldsymbol{F}$ being the deformation gradient. Here, $J = \det \boldsymbol{F}$ and $\bar{\boldsymbol{C}} = \bar{\boldsymbol{F}}^{\mathrm{T}}\bar{\boldsymbol{F}}$ represent the Jacobian, and the isochoric component of the right Cauchy-Green deformation tensor, respectively. Also, $\bar{\boldsymbol{F}}$ is the isochoric component of the deformation gradient and is defined as $\bar{\boldsymbol{F}} = J^{-1/3}\boldsymbol{F}$. According to the definition of elastic potential, the second Piola-Kirchhoff stress (PK2 stress) can be obtained as

$$\boldsymbol{S} = 2\frac{\partial W}{\partial \boldsymbol{C}} = 2\frac{\partial W_{\text{vol}}}{\partial \boldsymbol{C}} + 2\frac{\partial W_{\text{iso}}}{\partial \boldsymbol{C}} = \boldsymbol{S}_{\text{vol}} + \boldsymbol{S}_{\text{iso}}. \tag{40}$$

When the Mooney-Rivlin model, which is one of the simplest hyperelastic constitutive law, is chosen, the specific function forms of W_{vol} and W_{iso} are given by

$$W_{\text{vol}}(J) = \frac{1}{D}(J-1)^2, \tag{41}$$

$$W_{\text{iso}}\left(\bar{\boldsymbol{C}}\right) = C_1\left(\bar{I}_1 - 3\right) + C_2\left(\bar{I}_2 - 3\right) = W_{\text{iso}}\left(\bar{I}_1, \bar{I}_2\right). \tag{42}$$

Here, $\bar{I}_1$ and $\bar{I}_2$ represent the first and second invariables of $\bar{\boldsymbol{C}}$, which are respectively defined as

$$\bar{I}_1 = \mathrm{tr}\bar{\boldsymbol{C}}, \quad \bar{I}_2 = \frac{1}{2}\left(\mathrm{tr}^2\bar{\boldsymbol{C}} - \mathrm{tr}\bar{\boldsymbol{C}}^2\right), \tag{43}$$

where C_1 and C_2 are the material parameters. Then, the volumetric and isocholic parts of the 2nd Piola-Kirchhoff stress respectively given by

$$\boldsymbol{S}_{\text{vol}} = 2\frac{\partial W_{\text{vol}}(J)}{\partial \boldsymbol{C}} = J\frac{\partial W_{\text{vol}}}{\partial J}\boldsymbol{C}^{-1}, \tag{44}$$

$$\boldsymbol{S}_{\text{iso}} = 2\frac{\partial W_{\text{iso}}\left(\bar{I}_1, \bar{I}_2\right)}{\partial \boldsymbol{C}} = \left(2\frac{\partial W_{\text{iso}}}{\partial \bar{\boldsymbol{C}}}\right) : \frac{\partial \bar{\boldsymbol{C}}}{\partial \boldsymbol{C}}\left(J^{-2/3}\mathbb{Q}\right) : \left(2\frac{\partial W_{\text{iso}}}{\partial \bar{\boldsymbol{C}}}\right) = I_3^{-1/3}\mathbb{Q} : \bar{\boldsymbol{S}}, \tag{45}$$

where $I_3 = \det \boldsymbol{C}$. Also, $\mathbb{Q}$ and $\bar{\boldsymbol{S}}$ are respectively defined as

$$\mathbb{Q} = \mathbb{I} - \frac{1}{3}\boldsymbol{C}^{-1} \otimes \boldsymbol{C}, \tag{46}$$

$$\bar{\boldsymbol{S}} = 2\frac{\partial W_{\text{iso}}}{\partial \bar{\boldsymbol{C}}} = 2\frac{\partial W_{\text{iso}}}{\partial \bar{I}_1}\frac{\partial \bar{I}_1}{\partial \bar{\boldsymbol{C}}} + 2\frac{\partial W_{\text{iso}}}{\partial \bar{I}_2}\frac{\partial \bar{I}_2}{\partial \bar{\boldsymbol{C}}}. \tag{47}$$

Anisotropic versions of the above well-known isotropic hyperelastic model can be constructed just by adding the orientational dependency of the material behavior. Targeting at continuous-fiber-reinforced composite materials, Kaliske [30] and Kaliske and Schmidt [31] proposed the following stored strain energy function involving unit vectors $\boldsymbol{A}$ and $\boldsymbol{B}$ indicating the fiber orientations:

$$\Psi = W_{\text{vol}}(J) + W_{\text{iso}}\left(\bar{\boldsymbol{C}}, \boldsymbol{A}, \boldsymbol{B}\right). \tag{48}$$

Here, $W_{\text{vol}}(J)$ is the same as that in Equation (41), and $W_{\text{iso}}\left(\bar{\boldsymbol{C}}, \boldsymbol{A}, \boldsymbol{B}\right)$ is defined as

$$\begin{aligned} W_{\text{iso}}\left(\bar{\boldsymbol{C}}, \boldsymbol{A}, \boldsymbol{B}\right) &= W_{\text{iso}}\left(\bar{I}_1, \bar{I}_2, \bar{I}_4, \bar{I}_5, \bar{I}_6, \bar{I}_7, \bar{I}_8\right) \\ &= \sum_{i=1}^{3} a_i \left(\bar{I}_1 - 3\right)^i + \sum_{j=1}^{3} b_j \left(\bar{I}_2 - 3\right)^j + \sum_{k=2}^{6} c_k \left(\bar{I}_4 - 1\right)^k + \sum_{l=2}^{6} d_l \left(\bar{I}_5 - 1\right)^l \\ &\quad + \sum_{m=2}^{6} e_m \left(\bar{I}_6 - 1\right)^m + \sum_{n=2}^{6} f_n \left(\bar{I}_7 - 1\right)^n + \sum_{o=2}^{6} g_o \left(\bar{I}_8 - (\boldsymbol{A} \cdot \boldsymbol{B})^2\right)^o, \end{aligned} \tag{49}$$

along with the invariants of $\bar{\boldsymbol{C}}$

$$\bar{I}_4 = \boldsymbol{A} \cdot \bar{\boldsymbol{C}}\boldsymbol{A}, \quad \bar{I}_5 = \boldsymbol{A} \cdot \bar{\boldsymbol{C}}^2\boldsymbol{A}, \quad \bar{I}_6 = \boldsymbol{B} \cdot \bar{\boldsymbol{C}}\boldsymbol{B}, \quad \bar{I}_7 = \boldsymbol{B} \cdot \bar{\boldsymbol{C}}^2\boldsymbol{B}, \quad \bar{I}_8 = (\boldsymbol{A} \cdot \boldsymbol{B})\, \boldsymbol{A} \cdot \bar{\boldsymbol{C}}\boldsymbol{B}, \tag{50}$$

and the material parameters a_i, b_j, c_k, d_l, e_m, f_n and g_o.

In the context of the decoupling multiscale analysis with NMTs, the anisotropic hyperelastic constitutive equation presented above can be employed for the macroscopic material model, when constituents in a unit cell are Mooney-Rivlin materials. It is, however, to be noted that the applicability might be limited, especially when the unit cell cannot be regarded as a representative volume element for continuous-fiber-reinforced composites.

REFERENCES

1. Cadman JE, Zhou S, Chen Y, Li Q. On design of multi-functional microstructural materials. *Journal of Materials Science* 2013; 48:51–66.
2. Clausen A, Wang F, Jensen JS, Sigmund O, Lewis JA. Topology optimized architectures with programmable poisson's ratio over large deformations. *Advanced Materials* 2015; 27:5523–5527.
3. Zhao L, Ha S, Sharp KW, Geltmacher AB, Fonda RW, Kinsey AH, Zhang Y, Ryan SM, Erdeniz D, Dunand DC, Hemker KJ, Guest JK, Weihs TP. Permeability measurements and modeling of topology-optimized metallic 3-D woven lattices. *Acta Materialia* 2014; 81:326–336.
4. Brackett DJ, Ashcroft IA, Hague R. Topology optimization for additive manufacturing. 22nd Annual International Solid Freeform Fabrication Symposium, Texas, USA, pp. 348-362, 2011.
5. Gu W. On Challenges and Solutions of Topology Optimization for Aerospace Structural Design. 10th World Congress on Structural and Multidisciplinary Optimization. May 19-24, Orlando, Florida, USA, 2013.

6. Kennedy G. Large-scale multimaterial topology optimization for additive manufacturing. 56th AIAA/ASCE/AHS/ASC Structures, Structural Dynamics, and Materials Conference, AIAA SciTech, (AIAA 2015-1799). *American Institute of Aeronautics and Astronautics* 2015;1-13.
7. Zegard T, Paulino GH. Bridging topology optimization and additive manufacturing. *Structural and Multidisciplinary Optimization* 2015; DOI 10.1007/s00158-015-1274-4.
8. Sun SH, Koizumi Y, Kurosu S, Li YP, Chiba A. Effect of phase transformation on tensile behavior of Co-Cr-Mo alloy fabricated by electron-beam melting. *Funtai Oyobi Fummatsu Yakin/Journal of the Japan Society of Powder and Powder Metallurgy* 2014; 65(5):234–242.
9. Koizumi Y, Sun SH, Saito T, Kurosu S, Chiba A. Prototyping of Co-Cr-Mo alloy flat spiral spring by electron beam melting. *Funtai Oyobi Fummatsu Yakin/Journal of the Japan Society of Powder and Powder Metallurgy* 2014; 61(5):243–249.
10. Sun SH, Koizumi Y, Kurosu S, Li YP, Matsumoto H, Chiba A. Build direction dependence of microstructure and high-temperature tensile property of Co-Cr-Mo alloy fabricated by electron beam melting. *Acta Materialia* 2014; 64:154–168.
11. Sun SH, Koizumi Y, Kurosu S, Li YP, Chiba A. Phase and grain size inhomogeneity and their influences on creep behavior of Co-Cr-Mo alloy additive manufactured by electron beam melting. *Acta Materialia* 2015; 86:305-318.
12. Rodrigues H, Guedes JM, Bendsøe MP. Hierarchical optimization of material and structure. *Structural and Multidisciplinary Optimization* 2002; 24:1–10.
13. Yan J, Cheng GD, Liu L. A Uniform Optimum Material Based Model for Concurrent Optimization of Thermoelastic Structures and Materials. *International Journal for Simulation and Multidisciplinary Design Optimization* 2008; 2(4):259–266:103–110.
14. Niu B, Yan J, Chen G. Optimum structure with homogeneous optimum cellular material for maximum fundamental frequency. *Structural and Multidisciplinary Optimization* 2009; 39(2):115–132.
15. Sivapuram R, Dunning PD, Kim HA. Simultaneous material and structural optimization by multiscale topology optimization. *Structural and Multidisciplinary Optimization* 2016; online-published.
16. Xia L, Breitkopf P. Concurrent topology optimization design of material and structure within FE^2 nonlinear multiscale analysis framework. *Computer Methods in Applied Mechanics and Engineering* 2014; 278:524–542.
17. Xia L, Breitkopf P. Multiscale structural topology optimization with an approximate constitutive model for local material microstructure. *Computer Methods in Applied Mechanics and Engineering* 2015; 286:147–167.
18. Yan X, Huang X, Zha Y, Xie YM. Concurrent topology optimization of structures and their composite microstructures. *Computers & Structures* 2014; 133:103–110.
19. Feyel F, Chaboche JL. FE^2 multiscale approach for modelling the elastoviscoplastic behaviour of long fibre SiC/Ti composite materials. *Computer Methods in Applied Mechanics and Engineering* 2000; 183:309–330.
20. Smit RJM, Brekelmans WAM, Meijer HEH. Prediction of the mechanical behavior of nonlinear heterogeneous systems by multi-level finite element modeling. *Computer Methods in Applied Mechanics and Engineering* 1998;155:181–192.
21. Terada K, Kikuchi N. A class of general algorithms for multi-scale analyses of heterogeneous media. *Computer Methods in Applied Mechanics and Engineering* 2001; 190:5427–5464.
22. Zheng SF, Ding K, Denda M, Weng GJ. A dual homogenization and finite-element study on the in-plane local and global behavior of a nonlinear coated fiber composite. *Computer Methods in Applied Mechanics and Engineering* 2000; 183:141–155.
23. Nakshatrala PB, Tortorelli DA, Nakshatrala KB. Nonlinear structural design using multi scale topology optimization, Part I: Static formulation. *Computer Methods in Applied Mechanics and Engineering* 2013; 261–262:167–176.
24. Baaijens FPT, Kouznetsova V, Brekelmans WAM. An approach to micromacro modeling of heterogeneous materials. *Computational Mechanics* 2001; 27:37–48.
25. Simo JC, Taylor RL. Consistent tangent operators for rate-independent elastoplasticity. *Computer Methods in Applied Mechanics and Engineering* 1985; 48(1):101–118.
26. Kato J, Yachi D, Terada K, Kyoya T. Topology optimization of micro-structure for composites applying a decoupling multi-scale analysis. *Structural and Multidisciplinary Optimization* 2014; 49:595–608.
27. Watanabe I, Terada K. A method of predicting macroscopic yield strength of polycrystalline metals subjected to plastic forming by micro-macro de-coupling scheme. *International Journal of Mechanical Sciences* 2010; 52(2): 343–355.
28. Terada K, Kato J, Hirayama N, Inugai T, Yamamoto K. A method of two-scale analysis with micro-macro decoupling scheme: application to hyperelastic composite materials. *Computational Mechanics* 2013; 52:1199-1219.

29. Terada K, Hirayama N, Yamamoto K, Kato J, Kyoya T, Matsubara S, Arakawa Y, Ueno Y, Miyanaga N. Applicability of micro-macro decoupling scheme to two-scale analysis of fiber-reinforced plastics. *Advanced Composite Materials* 2014; 23(5–6):421-450.
30. Kaliske M, A formulation of elasticity and viscoelasticity for fiber reinforced material at small and finite strains. Computer Methods in Applied Mechanics and Engineering 2000; 185:225–243.
31. Kaliske M, Schmidt J. Nonlinear Anisotropic Elasticity at Finite Strains. *22nd CAD-FEM Users' Meeting 2004 International Congress on FEM Technology with ANSYS CFX & ICEM CFD Conference* 2004.
32. Storn R, Price K. Differential Evolution - A Simple and Efficient Heuristic for Global Optimization over Continuous Spaces. Journal of Global Optimization1997; 11:341–359.
33. Zhou M, Rozvany GIN. The COC algorithm, part II : Topological, geometrical and generalized shape optimization. *Computer Methods in Applied Mechanics and Engineering* 1991; 89:309–336.
34. Kato J, Lipka A, Ramm E. Multiphase material optimization for fiber reinforced composites with strain softening. *Structural and Multidisciplinary Optimization* 2009; 39:63–81.
35. Belytschko T, Liu WK, Moran B. *Nonlinear finite elements for continua and structures*. John Willey & Sons, Ltd. 2000.
36. Lasdon LS. *Optimization Theory for Large Systems*. The Macmillan Company 1970.
37. Patnaik SN, Guptill JD, Berke L. Merits and limitations of optimality criteria method for structural optimization. *International Journal for Numerical Methods in Engineering* 1995; 38:3087–3120.
38. Bendsøe MP, Sigmund O. *Topology optimization, theory, method and applications*. *Springer-Verlag* 2002.
39. Sigmund O, Pettersson J. Numerical instabilities in topology optimization: A survey on procedures dealing with checkerboards, mesh-dependencies and local minima. *Structural and Multidisciplinary Optimization* 1998; 16(1):68–75.
40. Buhl T, Pedersen CBW, Sigmund O. Stiffness design og geometrically nonlinear structures using topology optimization. *Structural and Multidisciplinary Optimization* 2000; 19:93–104.
41. Matsui K, Terada K, Nishiwaki S, Ishibashi Y. Consistent topology optimization method for structures with finite deformation. *Transactions of JSCES*, No.20010046, 2001.
42. Dijk van NP, Langelaar M, Keulen van F. Element deformation scaling for robust geometrically nonlinear analyses in topology optimization. *Structural and Multidisciplinary Optimization* 2014; 50:537–560.
43. Wang F, Lazarov BS, Sigmund O, Jensen JS. Interpolation scheme for fictitious domain techniques and topology optimization of finite strain elastic problems. *Computer Methods in Applied Mechanics and Engineering* 2014; 276:453–472.
44. Kemmler R, Lipka A, Ramm E. Large deformations and stability in topology optimization. *Structural and Multidisciplinary Optimization* 2005; 30:459–476.